

5.4 New Instruments and Techniques

5.4.1 Introduction

The development of beamline instrumentation and techniques that demonstrate and enhance the unique opportunities that are available at the Advanced Photon Source is undertaken primarily by XFD scientists and engineers working on the Synchrotron Radiation Instrumentation Collaborative Access Team (SRI-CAT) beamlines. As the facility has matured, the role of SRI-CAT has also evolved as reflected in our recently updated mission statement:

- To conduct R&D activities towards the improvement of IDs, standard components, high-heat-load optics, and other novel x-ray optical components and to develop innovative techniques useful to the entire community of APS CATs.
- To develop and implement strategic instrumentation programs that will open up new areas of research at the APS.
- To attract, educate, and foster new research communities in the uses for and applications of synchrotron radiation.

Testing of beamline components and x-ray optics and the development of novel experimental techniques primarily take place on those SRI-CAT beamlines that were designed with flexibility in mind. The beamlines designed to carry out specific

areas of technique development, called strategic instruments, have seen an increase in user demand as they have proceeded from the commissioning to the operational phase over the last year. Construction has begun on sector 4, for another strategic instrumentation program, namely the generation and use of variably polarized x-rays over the energy range of 0.5 to 100 keV. The sector 4-ID beamline will join those of sectors 2 and 3 to make up the complete set of the SRI-CAT strategic instrumentation programs:

- a milli-electron volt resolution instrument
- a micro-to-nano-electron volt instrument to perform nuclear resonant scattering experiments
- a 1-4 keV radiation source and instrumentation for use of coherent soft x-rays
- instrumentation for development of hard x-ray microfocusing optics and techniques
- a 0.5 keV to 100 keV variable polarization beamline

A schematic of the locations of these programs, along with the other major programs on the SRI-CAT beamlines, is shown in Fig. 5.28. Also indicated in Fig. 5.28 is a backscattering beamline (see section 5.2.3 for details). Because of the location of the 1-ID straight section with respect to other beamlines (i.e., there are no other beamlines immediately upstream), this beamline affords a unique opportunity for the development of a backscattering

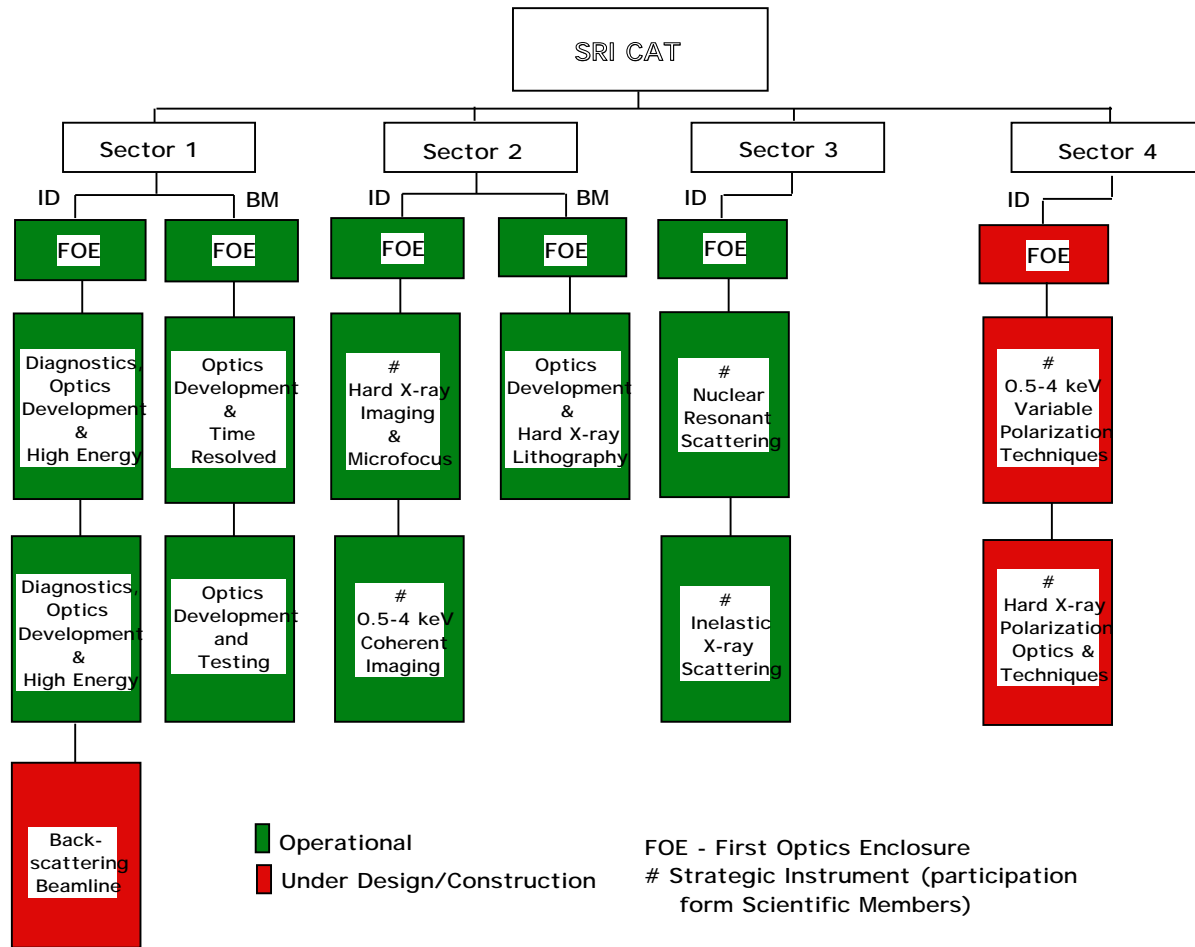


Fig. 5.28 Schematic of SRI-CAT showing activities and locations of various programs on the six beamlines.

beamline ($2\theta = 180^\circ$) by allowing the diffracted beam to pass back through the ID straight section and to emerge out the back end of the ID (see Fig. 5.12). Over the last year, the storage ring was fitted with a new vacuum chamber by ASD staff that would allow the backscattered beam to exit the vacuum chamber. A "back-end" was recently installed from the vacuum chamber port to a port through the storage ring tunnel. Development of the monochromator, which will be installed in 1-ID A/B, and experiment station, which will be located in the equipment assembly area, is currently

underway. This beamline will allow a detailed study of the physics of diffraction at exact backscattering geometry in addition to providing a beam of high resolution and large longitudinal coherence length in a nearly background-free environment.

The SRI-CAT staff have been active in making new scientific communities aware of the potential of the APS. One area to which the SRI-CAT beams have been put to use is the study of a variety of antiquities. Researchers from The Oriental Institute at The University of Chicago, the Field

Museum, and the Adler Planetarium (the latter two are both also located in Chicago, IL) have collaborated with the SRI-CAT staff in several feasibility studies to explore the potential application of synchrotron radiation to metallurgical and other studies relevant to archaeological and historical research.

5.4.2 Sector 1

1-BM Beamline and Optics

Numerous experiments have been conducted on beamline 1-BM starting with the observation of first light in March of 1995. Recently all the optical components have been put into place to permit operation of this beamline as originally designed. In many ways the optics on the 1-BM beamline are more complicated than those on some of the ID beamlines. The reason for this increased level of complication is that efficient use of a bending magnet beam absolutely requires focusing of the beam. In the following section, we summarize some of the commissioning activities that have occurred during the past year for the major optical components of the 1-BM beamline. In particular, we concentrate on the properties of the doubly focused beam entering the 1-BM-C station.

The first major optical component on the beamline is a water-cooled 1.2-m-long palladium-coated mirror. This flat mirror, bendable to a cylindrical shape, is used to vertically collimate the beam (i.e., focus the beam at infinity). Collimating the beam allows the user to accept a larger vertical beam without sacrificing energy resolution, because all the rays in the beam after the

mirror will make an identical angle with any monochromator crystal further downstream. Commissioning activities associated with this mirror were concentrated on the measurement of the decrease in the energy resolution, E/E . These measurements were made using a highly dispersive Si analyzer crystal in the beam after the monochromator to monitor E/E as the mirror figure was changed from flat to collimating. Measurements at 10 keV showed that the bandwidth passed by the monochromator for a 2.5-mm vertical beam 22.9 m from the source decreased from 5.5×10^{-4} to 1.5×10^{-4} for the Si (111) reflection and from 3.6×10^{-4} to 8.1×10^{-5} for Si (220). The lower values on the energy resolution are only 15% and 25% that expected for perfect collimation. The discrepancy can likely be accounted for by residual fabrication slope errors in the mirror. Later measurements demonstrated that, while the central 0.8 m of the mirror had only 2-3 microrad deviations from an ideal bend, both of the edges of the mirror were substantially overbent to 10 microrads. Thus by using a smaller beam the theoretical resolution can be approached, albeit with a loss in flux.

The collimating mirror is followed by the double-crystal monochromator (DCM). This monochromator has been used quite extensively over the past year but has recently been improved by the installation of a sagittally bent second crystal, which provides horizontal focusing of the beam into the C-station. Initial tests of this sagittal focusing crystal, designed following the "golden ratio" concept put forth by Kushnir et al. (1993), have been quite promising. A horizontal focus of 0.45 mm was achieved at 10 keV for a 72-mm-wide beam incident on the monochromator using the Si (220) reflection. Furthermore, this focal size was achieved with a broadening of the

monochromator crystal rocking curve only 25% above that of the ideal case for a flat crystal.

The third and final major optical component in the beamline is a 1-m-long, palladium-coated mirror located between the B- and C-stations. This mirror, also a flat mirror bendable to a cylinder, provides vertical focusing of the beam for the C-station. The measured vertical size of the beam from this mirror was 108 microns, which is only 20% above an ideal image expected from ray tracing the source. Although we were able to achieve a good focus with this mirror, a great deal of structure (horizontal striations) was observed in the unfocused beam. After several tests, it was determined that the structure arose from 2-3 microradian fabrication slope errors. One should note that, for a mirror of this size, slope errors in this range are at the limit of current mirror polishing technology. Although the collimating mirror on the beamline did not display structure as dramatic as this, several other mirrors at APS beamlines have exhibited similar features. Features such as these are much more readily observable at the APS, as opposed to at other synchrotrons, due to the small source size coupled with the availability of long beamlines at the APS.

A summary of the combined performance of all the 1-BM optics is contained in Fig. 5.29 and Table 5.5. Figure 5.29 shows a doubly focused 9.0 keV beam in the C-station using a Si (111) monochromator. This focal spot size was attained using a $60 \times 2.5 \text{ mm}^2$ beam incident on the monochromator. Profiles of this image give full-width half-maximum (FWHM) values of 0.25 mm vertical and 0.60 mm horizontal, which are roughly twice as large as expected for ideal

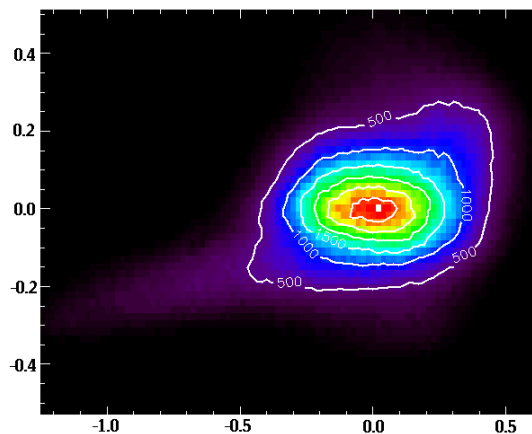


Fig. 5.29 Doubly focused beam in the 1-BM-C station with a $72 \times 2.5 \text{ mm}^2$ beam incident on the sagittally focusing Si (111) monochromator.

optics. The increase in the vertical spot size compared to that taken with flat crystal optics is believed to be due to aberrations induced by a slight twisting in the sagittal crystal. While the increase in the horizontal spot size is probably due to nonuniformities in the thickness of the bending crystal. New crystals are currently being fabricated to improve the focusing qualities. Table 5.5 lists the achieved photon fluxes and bandwidths into the C-station when using a $50 \times 2.5 \text{ mm}^2$ beam, 22.9 m from the source, and it gives the percentage of these values compared to the ideal case of perfect optics.

It should be pointed out that the flux value measured on beamline 1-BM is within a factor of 10 of the flux obtained from an unfocused ID beam. Furthermore, because of the collimation of the beam prior to the monochromator, the bandwidths on 1-BM are nearly the same as those seen on the ID beamlines. This demonstrates that, by properly designing the optics on a bending magnet source at the APS and for experiments that require only a large

Table 5.5 Photon Fluxes and Bandwidths Achieved in the 1-BM-C Station.

Mono Crystal	Flux (ph/s/100mA)	Percentage of Ideal	E/E	Percentage of Ideal
Si (111) (9 keV)	1.3×10^{12}	72%	1.5×10^{-4}	115%
Si (220) (10 keV)	5.0×10^{11}	65%	8.1×10^{-5}	125%

incident flux on the sample with relaxed conditions on beam brilliance, a BM beamline can be a viable alternative to an ID beamline. As of July 1, 1998, this beamline has been assigned operational status.

1-ID Beamline and Optics

The 1-ID beamline is fully commissioned and has been operating with users (including independent investigators) throughout the last year. The only major change to the beamline configuration is that L1 white-beam slits were installed. Previously, temporary white-beam slits were used. The installation of the L1 slits completes the installation of standard components for 1-ID.

An 8-circle Huber diffractometer has been temporarily installed in the 1-ID-C experiment station. This diffractometer was purchased for sector 4 and will be moved when that beamline is ready for operations, but until then it will be used on 1-ID. The addition of the 8-circle (replacing the standard 6-circle) diffractometer greatly increases the capability of the beamline to study off-specular reflectivity and other out-of-plane scattering phenomena.

The 1-ID beamline is, in part, a test bed for optics development. Installation and testing

of crystals and other optical components has been a frequent occurrence over the past year and will continue into the foreseeable future. During the past year, 1-ID has had three different optical configurations. For experiments in the 6-18 keV range, Si (111) crystals are installed into the Kohzu DCM. For the energy range of 9-45 keV, Si (311) crystals are installed into the Kohzu DCM. In addition to giving the higher energy range, this configuration has an energy bandpass roughly 20% of the Si (111) (with corresponding reduction in intensity), which is particularly useful for studies of anomalous diffraction for elements with K-edges in the 20-45 keV range. The final configuration is for experiments requiring photons in the 40-150 keV region. For this energy range, an auxiliary monochromator is installed in 1-ID-B. The first crystal in this monochromator is cooled with liquid nitrogen and resides inside a large vacuum chamber. The second crystal is not cooled and is placed outside the vacuum chamber. This arrangement allows for large crystal separations (up to a meter) and, as a consequence, the standard 35-mm offset between white and monochromatic beam can be obtained for energies up to 150 keV. With such an offset, the high-energy monochromatic beam can be brought into 1-ID-C allowing for very low background levels as compared with working in the same station with the monochromator.

After several years of operation cooling the silicon monochromators with liquid nitrogen, we are pleased with the performance of this system (Kohzu monochromator, crystals, liquid nitrogen pump, etc.). Nonetheless, two improvements for the monochromator were tested on the 1-ID line last year: cooling the second crystal to reduce beam motion as a function of energy and adding a sagittally focusing second crystal. (Both these activities are described in more detail in section 5.3.)

In collaboration with the sector 2 microfocusing effort, zone plates for focusing at 40 keV were tested at 1-ID. The zone plates used for this study were designed to produce a phase shift at 20 keV (i.e., $\lambda/2$ at 40 keV). They were made of gold with a thickness of 3.3 microns, had an outer zone width of 0.3 microns, an overall diameter of 80 microns, and a focusing distance of 1 m (at 40 keV). From one zone plate, a focus beam size of 2.5 microns by 8 microns (vertically and horizontally, respectively) was achieved with an efficiency of 19%. This is essentially the theoretical efficiency for the system tested. To increase the efficiency, a second zone plate was “stacked” with the first to give a total of phase shift at 40 keV. The efficiency of this system was measured to be 38%, showing that the two zone plates could be aligned well enough to add in phase with each other. The total flux density gain of the stacked zone plates was a factor of 120.

Hard X-ray Polarization Program

The objective of this program is to develop instrumentation and techniques suitable for performing investigations of magnetic systems. During the previous years, effort

was directed toward evaluating phase-retarding crystal optics. These accomplishments were described in the XFD *Progress Report* 1996-97. During 1997-98, the focus has been to demonstrate unique magnetic measurements using the phase-retarding crystal optics. In the following, some of the early results from these scientific research studies are described.

A study of the magnetic properties of Fe/Gd multilayers has been carried out during several runs on beamline 1-ID. These studies began as an investigation of the spin structures of the Fe and Gd layers as a function of temperature and applied magnetic field. More recently, the studies have been expanded to include measurements of magnetic roughness of the multilayers by using spin-sensitive diffuse scattering.

The Fe/Gd multilayers are fundamentally an exciting system to study because they exhibit a variety of spin structures, as can be seen in the temperature-field phase diagram of Fig. 5.30 (LePage and Camley, 1990). The Fe and Gd layers couple antiferromagnetically and, at low applied fields, are Gd-aligned (at low temperatures where the Gd moment is dominant) or Fe-aligned (above the compensation temperature where the Fe moment is dominant). Due to the competition between the Zeeman and exchange energies, there are also bulk- and surface-twisted phases for larger applied magnetic fields. In addition to the rich phase diagram, the existence of surface and bulk magnetic structures makes the Fe/Gd multilayers an excellent model system to study surface magnetic reconstruction problems, i.e., how a spin configuration at the surface may differ from the bulk spin configuration. This is analogous to the crystal surface

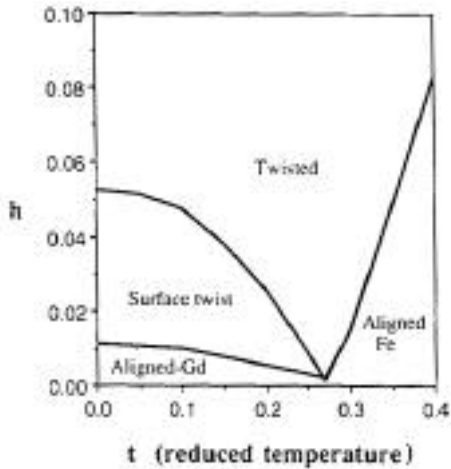


Fig. 5.30 Calculated phase diagram for a Fe/Gd multilayer. The axes are in units of reduced temperature (T/TC for TC of Fe) and field ($H/JSFe$). [Reprinted with permission from LePage and Camley, *Phys. Rev. Lett.* 65 (1990) 1152.]

reconstruction that has been widely studied in recent years.

The Fe/Gd multilayers are also a useful system for studies of magnetic roughness—including vertical and in-plane correlation lengths—in multilayers. This is an extremely important issue in technological applications in which spin transport effects are utilized (e.g., the giant magneto-resistance effect) because the size of the effect is directly related to the in-plane magnetic roughness. Magnetic roughness measurements to date have been confined to transition metal samples consisting of no more than a few layers because of the necessity of using low-energy x-rays for resonant enhancement at transition metal L edges. But by using a rare-earth sample (with L edges in the hard x-ray regime) and high-intensity undulator radiation, the entire multilayer can be probed.

Both the spin structure and magnetic roughness were studied using resonant x-ray magnetic scattering—at the Gd L_3 and Fe K edges for the spin structure measurements and at the Gd L_3 edge for the magnetic roughness measurements. The magnetic information was extracted from specular reflectivity and diffuse scattering measurements by subtracting data sets that differ only by having opposite photon helicities. A diamond (111) phase retarder produced the required circularly polarized photons, and the helicity was switched by rotating the retarder by a fixed amount to either side of the Bragg peak. The sample was placed between the poles of a permanent magnet, and the sample and magnet were mounted in a closed-cycle helium refrigerator in order to explore a range of sample temperatures.

A comprehensive set of spin structure measurements has been completed for an applied field of 2.4 kG. Due to the fact that resonant x-ray magnetic scattering is only sensitive to magnetization in the scattering plane, data were collected with two relative orientations of the field—parallel and perpendicular to the scattering plane—at each temperature in order to differentiate between aligned and twisted phases. The difference signal for the perpendicular orientation was observed to disappear in the temperature range of 160-180 K (see Fig. 5.31), indicating a phase transition from twisted to aligned. One other notable feature of the data was the sign change of the difference signal as a function of superlattice Bragg peak, which was seen at the Gd L_3 edge but not at the Fe K edge. From simulations, such sign flipping can be accounted for by nonuniformity of the Gd moment within a given layer. This explanation also agrees with theoretical calculations (Camley, 1989) in which

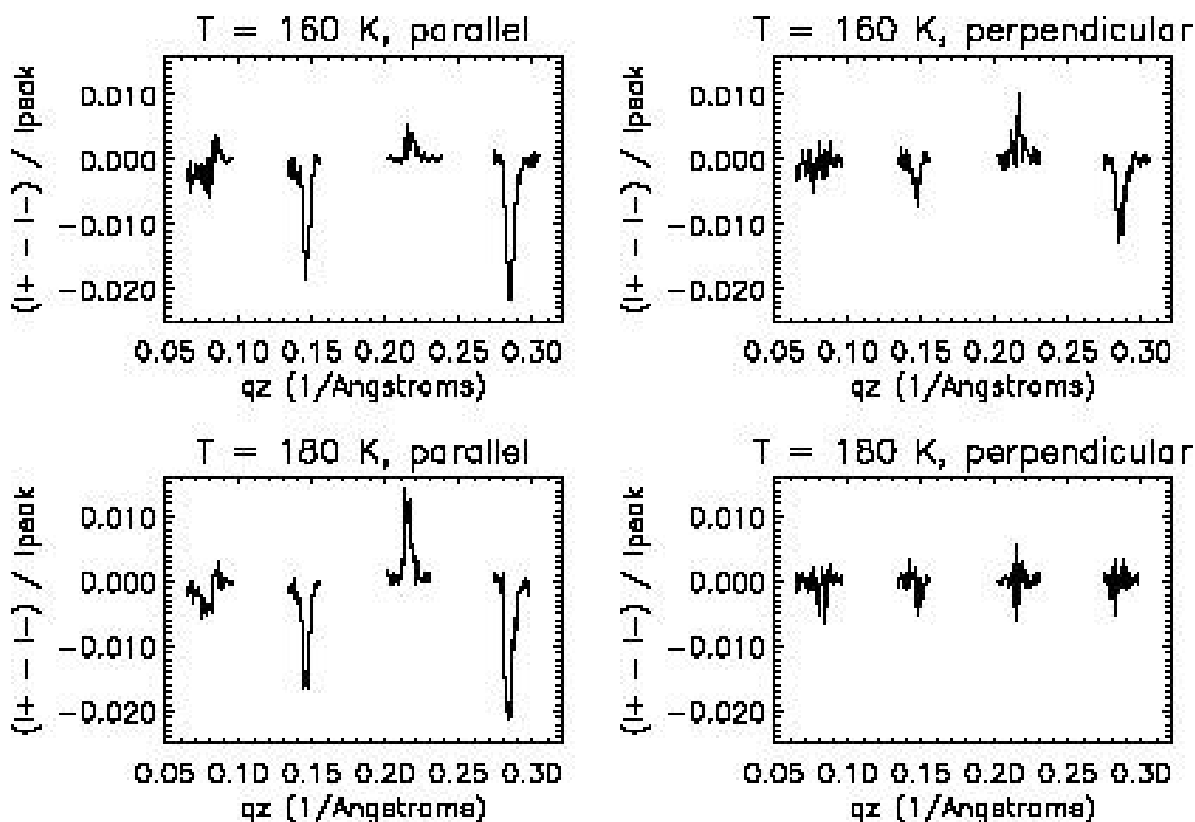


Fig. 5.31 Magnetic reflectivity data collected at the Gd L_3 edge at temperatures of 160 K and 180 K. The difference signal between the reflectivity measured with opposite photon helicities divided by the summed signal at the superlattice Bragg peak is plotted. Note the disappearance of the difference signal for the perpendicular relative orientation (i.e., the field is applied perpendicular to the scattering plane) at 180 K, indicating that the multilayer is in an aligned phase.

interface coupling of the Fe and Gd atoms results in either an enhanced or reduced Gd moment at the interface as compared to in the bulk of the layer, depending upon the strength of the interface coupling. In contrast, a lack of sign flipping in the data collected at the Fe K edge suggests uniformity of the Fe moment within each layer.

Spin-sensitive magnetic diffuse scattering measurements have been made for an Fe-aligned phase of the Fe/Gd multilayer in

an applied field of 3.4 kG. Magnetic diffuse scattering is a very weak process, so reasonable statistics have only been collected for two transverse scans (which give information about in-plane magnetic correlations) and an offset scan in which the sample was rotated 0.12 degrees away from specular (which gives information about out-of-plane magnetic correlations). These three data sets are extremely rich—even showing features in the magnetic signal corresponding in reciprocal space to multiple scattering events in the charge scattering—and, for a complete analysis,

will require an extension of the distorted wave Born approximation into the resonant magnetic regime.

The polarization studies have also included work on x-ray magnetic circular dichroism (XMCD) in REFe₂ compounds (RE = rare earth) as part of an ongoing study of the temperature dependence of XMCD in rare earth-transition metal materials. The goal of these measurements has been to measure the different magnetic exchange couplings in these compounds and plot their variation with temperature. An understanding of the exchange couplings that control the magnetization of the 5d band is essential in the development of new magnetic materials. The strength of the exchange couplings can be extracted from XMCD spectra by measuring the variation of the features in the dichroic spectra with temperature. Each feature, in principle, can be correlated with a specific electronic orbital state in the compound. Figure 5.32 shows a measurement of two such spectra taken at the Tm L₃ edge of TmFe₂. The sign of the XMCD spectra is inverted upon raising the temperature because the material goes through the compensation point where the dominant magnetization sublattice of the

sample changes from Tm to Fe. Tm is an interesting compound, since in addition to features A and C, which we showed in a previous study to arise from quadrupolar and dipolar transitions to rare earth 4f and 5d states, respectively, it possesses a feature (B) that becomes larger with temperature. The origin of this feature, which is not as prominent in other rare earths in the REFe₂ series, is still uncertain, but our study suggests that it might arise from a hybridization of Tm 5d states with the Fe 3d states.

These measurements utilized the diamond phase-retarding optics developed here at the APS. The use of these optics has proved essential for these types of experiments due to the difficulty of reversing the sample magnetization in cryogenic environments.

The sample investigations of magnetic systems reflect a need for a dedicated beamline for such studies utilizing x-ray polarization techniques. This need has led SRI-CAT to plan sector 4, which is dedicated to the development of new polarization instruments and techniques.

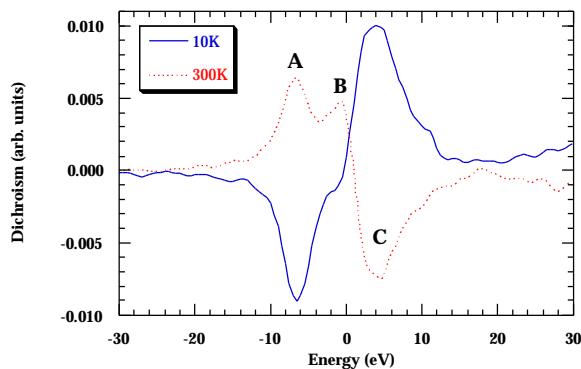


Fig. 5.32 Dichroism signal measured at the Tm L₃ edge of TmFe₂ at 10 K and 300 K.

Time-Resolved Program

As part of the time-resolved program in XFD, we are developing three classes of high-speed x-ray beam choppers or shutters. These beam choppers will span ten decades of time resolution and will offer a variable time between pulses.

The first class of beam chopper is based upon a commercial solenoid operating as a linear shutter. This design will cover the open time window range from a second to less than 1 millisecond. The desired

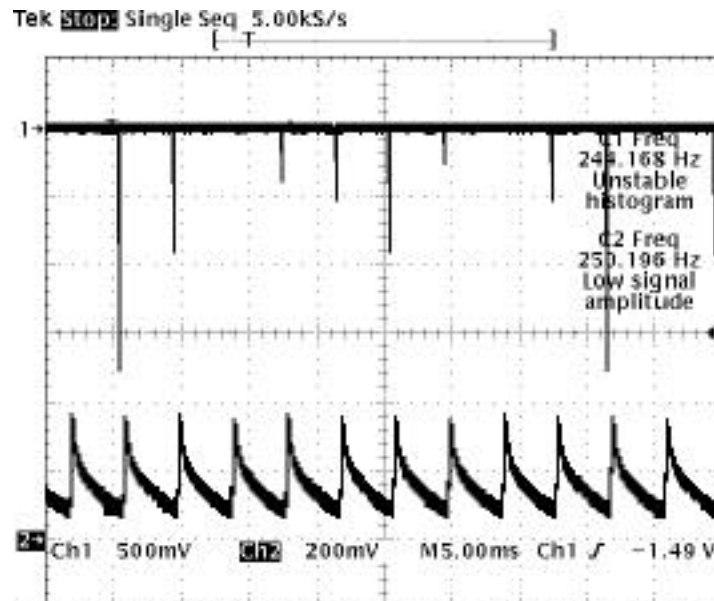
operating parameters are two fold. First, a linear motion of the solenoid plunger, which can open or close an aperture quickly, on the order of 1 to 2 ms, and remain open or closed for a period varying from 20 ms to a second. The maximum operation rate would be 50 Hz. Second, we want a system that can open and close the time window on the order of 300 microseconds and remain closed for an unspecified time. Both of these designs depend upon the driving power supply. A pulsed high-voltage (400 V) high-current (5 A) power supply is being developed in house to drive the solenoid beam choppers. They will be used with the charge coupled device (CCD) camera detectors and high-speed beam chopper described below.

The next class of beam chopper is also based upon a commercial product, namely a high-speed line scanner. The central component for this device is a high-speed (80000 RPM) rotating beryllium cylinder with a narrow slot through the center that can rotate synchronously with respect to the orbital frequency of the storage ring. The large numerical aperture of the slot forms a fixed open time window of about 2.65 microseconds. (The close time is about 300 microseconds, hence the need for the fast solenoid shutter described above for applications requiring a longer close time.) Pulses shorter than 2.65 microseconds would require selective loading patterns of the APS storage ring, but in general, x-ray pulses as short as 75 psec, corresponding to a single bunch of stored particles, could be achieved with this synchronously operated beam chopper. Delivery of this item is expected in the fall of 1998.

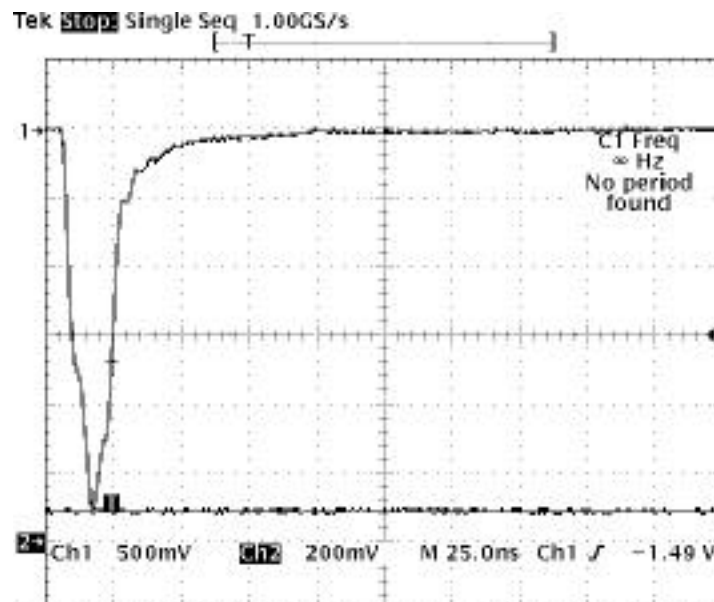
The final class of beam chopper consists of a rotating Si crystal cube. In the normal fill pattern of the APS storage ring, about two

thirds of the ring is filled, usually with about 25 bunches. The time between these bunches is typically about 100 - 150 ns (depends on the exact fill pattern). For certain time-resolved experiments, the ability to change this time structure is desirable. In particular, a longer inter-bunch time may be useful. With a rotating crystal, we have demonstrated that it is possible to increase the time between x-ray bursts. By using a 15-mm silicon cube mounted on a Stanford Research Instruments SR 540 beam chopper motor, we were able to take advantage of the small Darwin width opening angle of the crystal as a fast shutter for a monochromatic beam. The crystal was cut so that there were four Si (220) reflecting surfaces available. Depending on the speed of the crystal rotation, monochromatic x-ray bursts with varying interburst times from about 1 second to 250 msec were achieved. In the first case, the length of the x-ray burst is actually the entire fill pattern of the synchrotron ring ($\sim 2.5 \mu\text{sec}$); while in the latter case, the length of the x-ray burst is actually one individual pulse ($\sim 100 \text{ ps}$) from the fill pattern. In this initial demonstration, the rotating crystal chopper was operated asynchronously with the storage ring period (Fig. 5.33). In order to be a more useful instrument, the rotating crystal chopper must be able to operate synchronously with the storage ring. We are currently looking into improvements of the rotation devices that will permit synchronous operations.

The other main area of instrumentation development ongoing in the time-resolved program involves a high-speed digital CCD camera. During the last year, the software for operating the camera has been improved significantly. The following aspects have been added or enhanced: user friendliness, ability of executing loop commands within



(a)



(b)

Fig. 5.33 In (a), the lower trace is from an optical diode, which measures the frequency of the rotating cube, and the upper trace is from an avalanche photodiode (APD) x-ray detector. This figure shows that the x-rays are now arriving at about 250 Hz. (The crystal is actually rotating at about 63 Hz, but there are four reflecting faces available.) The asynchronous operation of the chopper results in variable x-ray pulse amplitudes (and sometimes misses them altogether). Figure (b) shows that each x-ray pulse shown in (a) is actually a single bunch (out of typically 25 bunches) from the synchrotron. In this case, the captured bunch is a sextet, which is normally followed by a triplet about 100 ns later. The triplet does not show up because the opening transmission time of the crystal is less than 100 ns at this rotation frequency.

the script language, synchronization between the camera and other user instruments, such as rapid mixer and stopped-flow devices. Full characterization of the CCD camera, including measurements on time response and x-ray detection efficiency is in progress.

High-Energy X-ray Scattering

This program focuses on the development of instruments and techniques that utilize x-rays in the energy range from about 20 keV to 200 keV. Many aspects of instrumentation (on 1-BM) were described in the *XFD Progress Report 1996-97*. The unique capabilities of this beamline have attracted many scientists to perform numerous materials science studies during 1997-98. In the following, we present a brief summary of these measurements.

Several experiments were conducted in which high-energy x-rays were used to study noncrystalline materials. For these experiments, the bent-crystal monochromator (BCM) in 1-BM-B was used to produce an x-ray beam with an energy of 61 keV. The BCM consists of one long crystal of either (111) or (220) oriented silicon that is bent (meridionally) to horizontally focus the beam. The crystal was cut to have an asymmetry that allowed for a monochromatic focus within the 1-BM-B station for energies greater than 50 keV. The diffractometer was operated in a vertical scanning geometry to take advantage of the superior angular divergence in that direction. With the use of the BCM, the typical time to complete a scan on an amorphous material sample was around one hour. This configuration is a significant improvement over the setups used for previous

experiments on amorphous or liquid materials.

In collaboration with scientists from the University of Missouri-Rolla and MSD at Argonne, we examined a series of depleted uranium oxide glass alloys. Glass alloys such as these are candidates for nuclear waste storage and, hence, knowledge of the structure of such materials is crucial to understanding its long-term stability. The glasses studied were iron phosphate glasses alloyed with various amounts of uranium oxide ranging from 0% to 24.5 wt.%. Figure 5.34 shows the scattering from three of the glass alloys. The effect of UO_2 composition upon the scattering is dramatic, as might be expected considering the heavy weighting of uranium in the x-ray scattering. Figure 5.35 shows the total correlation function, $T(r)$ for data collected with high-energy x-rays and with neutrons. The enhanced contribution to the x-ray $T(r)$ by uranium is clearly evident. These results are being used in combination with Raman, Mossbauer, and x-ray absorption spectroscopy to help resolve structural issues for these glass alloys (Marasinghe et al., 1998).

Another study was conducted in collaboration with scientists from MSD at Argonne and the Osaka Institute of Technology. Glass pellets of GeO_2 were post-processed by compression and heating to achieve densities of 4.08 and 4.18 g/cm^3 (normal density for GeO_2 is 3.62 g/cm^3). The long-range network topology of glasses in general is a subject of interest. Studying the compression-induced change in the scattering from GeO_2 was intended to provide insight into this matter, as well as into the rigidity of bond-angle-dependent potentials. Scattering from the two high-density samples and from a normal density sample is shown in Fig. 5.36, which shows

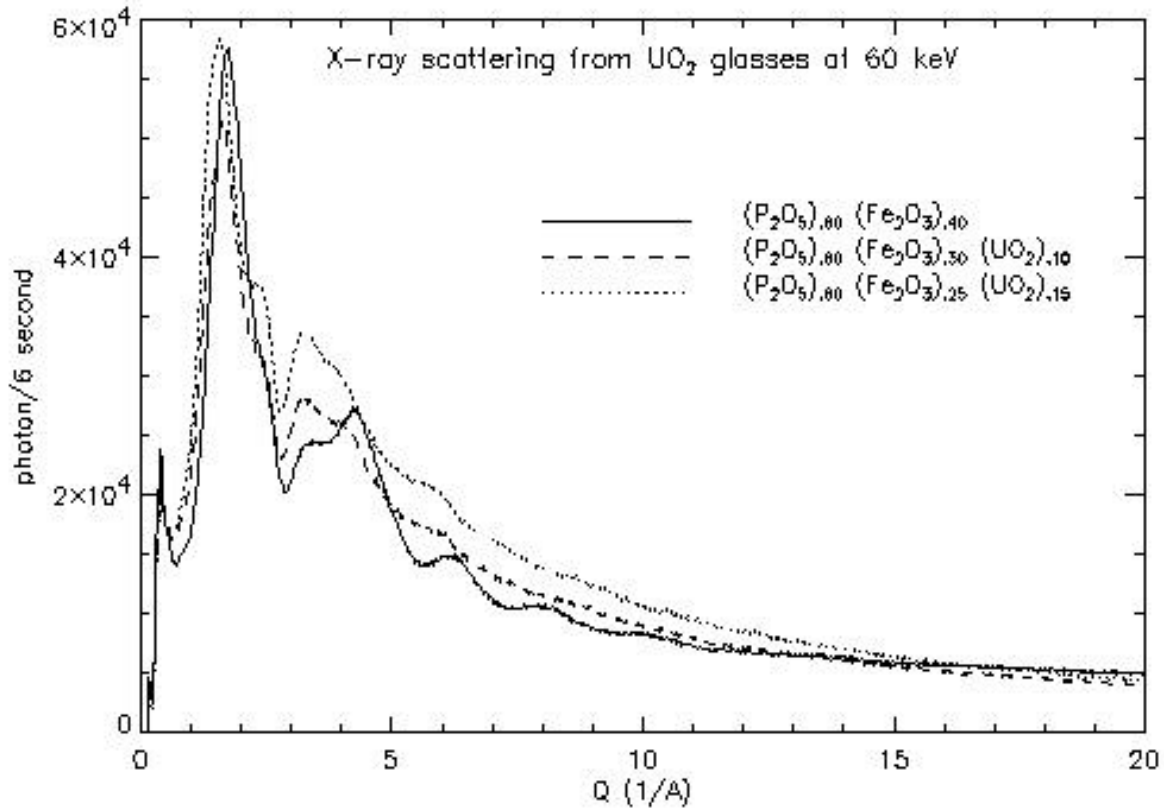


Fig. 5.34 The x-ray scattering for three glasses with different UO_2 compositions.

the high Q scattering ($Q=4 \sin \theta / \lambda$) data for the uncompressed sample. Structure is readily apparent out to at least 20 \AA^{-1} , indicating the utility of high-energy x-rays to collect scattering out to high Q . The $T(r)$ for these samples is shown in Fig. 5.37. From these results, we see that the first two shells are largely unchanged by the compression, but that significant differences exist for shells past the first two.

With a group of scientists from Indiana University, we studied the structure of alkali tellurite glasses. These glasses have the general formula $(Na_2O)_x(TeO_2)_{1-x}$, where TeO_2 is the glass former and Na_2O is the modifier. Varying the concentration of the latter controls bulk properties, such as the

glass-forming temperature and nonlinear optical response. The strong nonlinear optical response, which arises from a polarizable lone Te electron pair, combined with the good chemical durability and transparency in the visible and near infra-red (IR) ranges, makes these glasses a candidate for photonics applications. From previous results obtained by neutron scattering and from nuclear magnetic resonance experiments, structural models had been developed but without sufficient information to determine which was correct for any given composition. By adding the results from the high-energy x-ray scattering experiments to their other results, the Reverse Monte Carlo algorithm was used to give estimates on compositions for various

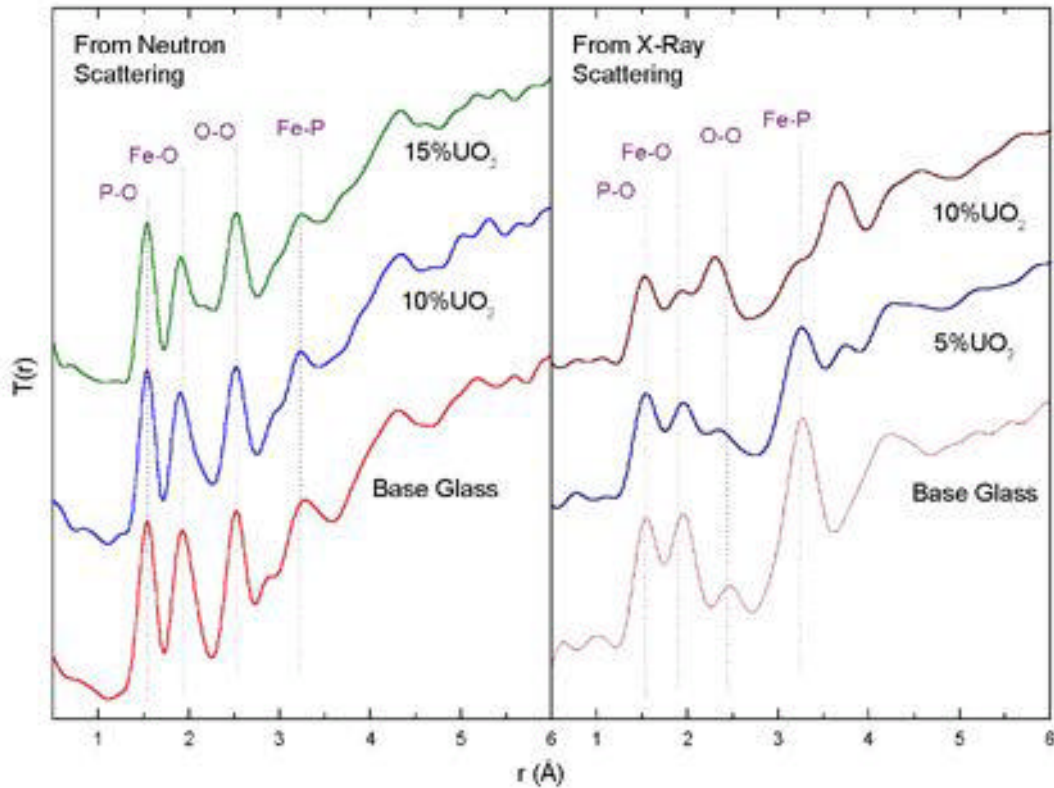


Fig. 5.35 The total correlation function derived from neutron and x-ray scattering for three glasses with different UO_2 compositions.

structural components (McLaughlin et al., 1998).

The high-energy scattering capability provided at beamline 1-BM is unique, and many scientists have taken advantage of it to study materials science problems requiring x-ray scattering data for full understanding.

5.4.3 Sector 2

2-BM Beamline and Optics

The 2-BM beamline, consisting of a bending magnet source and the 2-BM-A and 2-BM-B

experiment stations, has been commissioned and operational since the end of 1997. The beamline as a whole has demonstrated excellent performance. The last major optical component to be installed was the M2 mirror in 2-BM-B, a 1.2-m-long Si flat, side-cooled mirror with Si, Rh, and Pt stripes on its reflective surface for broadband energy selection up to ~ 35 keV. This mirror and its cousin in 2-BM-A have performed very well, demonstrating reflectivity curves that are within 5% of the expected theoretical reflectivities. The last remaining optical component to be installed as per the *Sector 2 Final Design Report* is a double-multilayer monochromator (DMM) for medium-bandwidth energy selection.

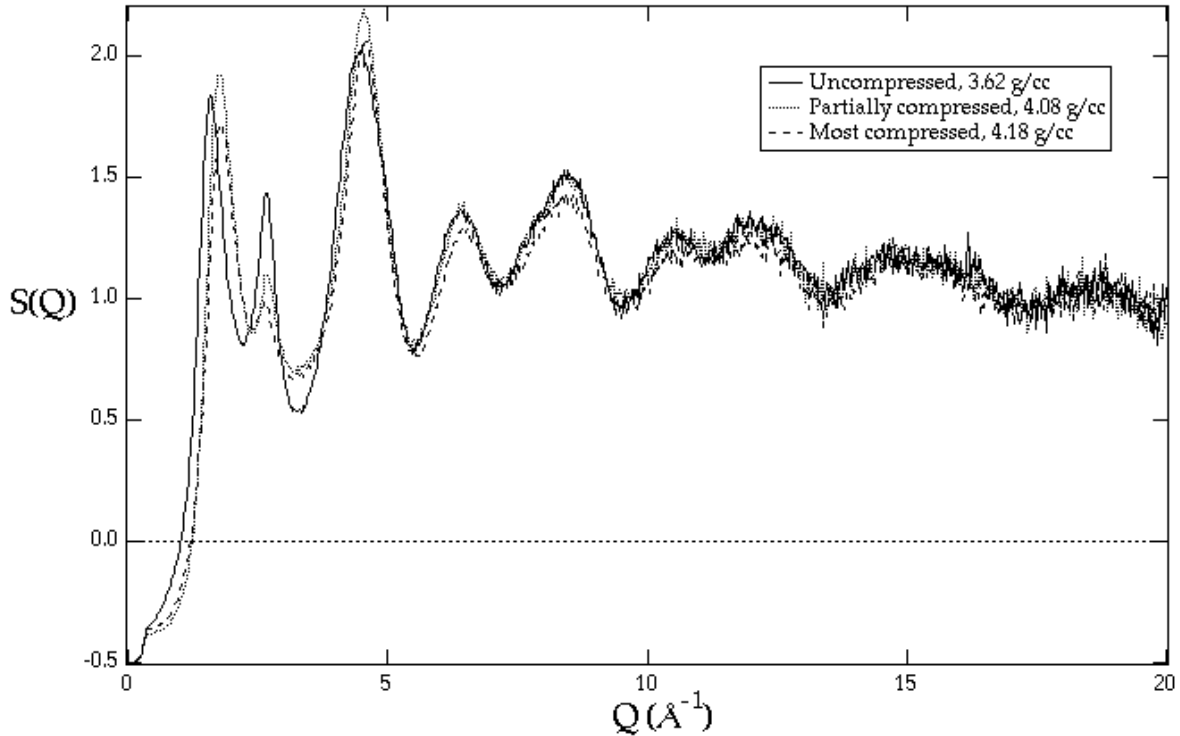


Fig. 5.36 The x-ray structure factor for normal GeO_2 glass and for two densified GeO_2 glasses.

This instrument is slated to be commissioned in October 1998.

Optics Characterization and Advanced Technique Development

Significant progress has been made at 2-BM-B on testing and characterization of zone plate lenses for high-resolution focusing of x-rays and on development of replicable x-ray multilayer optics. For microfocusing applications with high-energy x-rays, zone plates can be stacked together to increase their efficiency. By precisely aligning two zone plates optimized for 8 keV x-rays, we showed that they can constructively interfere with one another and produce a combined efficiency of >30% for

16 keV x-rays, which is close to the optimal value that can be achieved for a zone plate with rectangular profile. At 2-BM-B, we have also made measurements of the reflectivity and scattering from multilayers on Ni-electroform substrates for x-ray astronomy applications. These data were compared with AFM and WYCO roughness measurement to assess their validity at different spatial frequencies. The results showed that precise replicas of a master mirror surface can be made repeatedly by electroforming followed by liftoff from the master.

On the advanced technique development front, we have assembled and tested instrumentation for microtomography experiments that uses a high-spatial-resolution CCD camera. Either absorption or

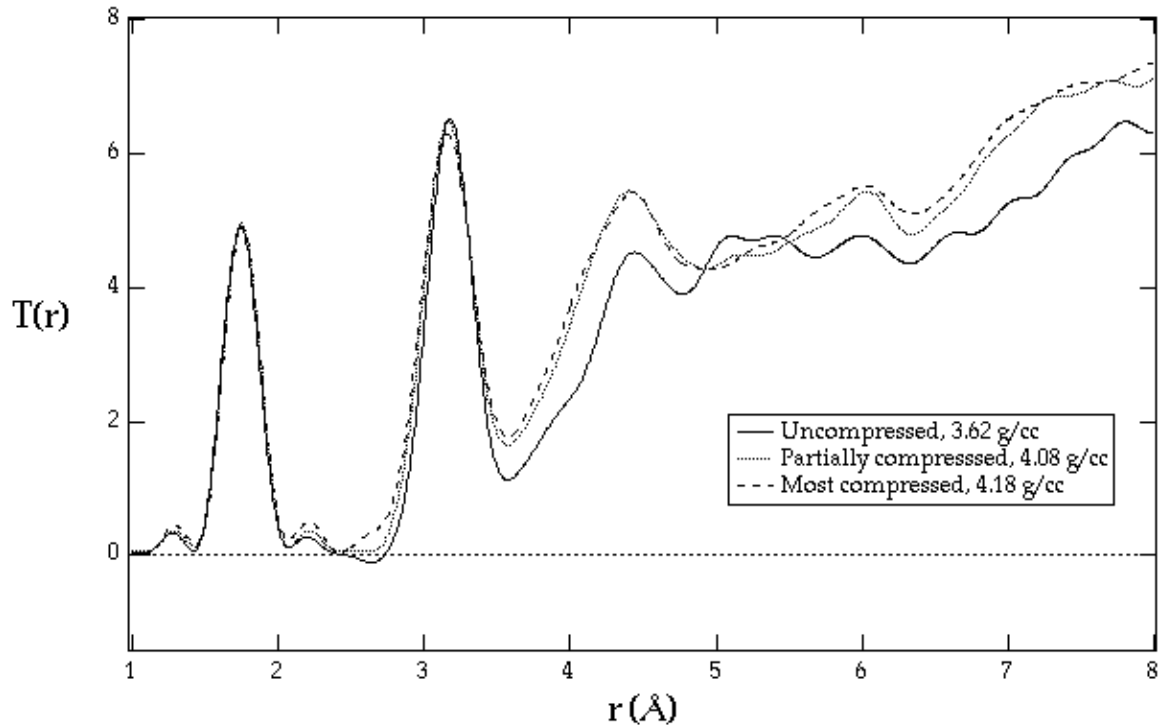


Fig. 5.37 The total correlation function for normal GeO_2 glass and for two densified GeO_2 glasses.

phase contrast images of the sample can be obtained with this instrumentation. Fast data collection (~ 1 projection/s) is achieved with a sample rotation angle range of 180° . Using the filtered back-projection algorithm to reconstruct the tomographic data, we demonstrated a resolution of $1\text{-}2\ \mu\text{m}$ in all three spatial dimensions. In collaboration with the ANL Environmental Research Division (ER), properties of soil aggregates, such as density distribution, porosity, and connectivity of pores, were studied using the microtomography setup (Fig. 5.38). The structure of soil samples ($\sim 1\ \text{mm}$ in size) from different field locations and the mechanism of soil expansion and contraction by hydrated ions were examined. X-ray tomography provided repeated

nondestructive evaluations of the sample throughout the wetting and drying cycles.

Deep X-ray Lithography

The deep x-ray lithography (DXRL) program at 2-BM has been highly successful in the last year. Among the more notable achievements, we developed new mask technology that is especially suitable for DXRL. The mask technology uses 1-mm beryllium wafers as substrates, with either silicon nitride or boron coatings to act as adhesion and protection layers. We have completed finite element analysis modeling that shows the 1-mm beryllium wafers to be most suitable for both thermal management

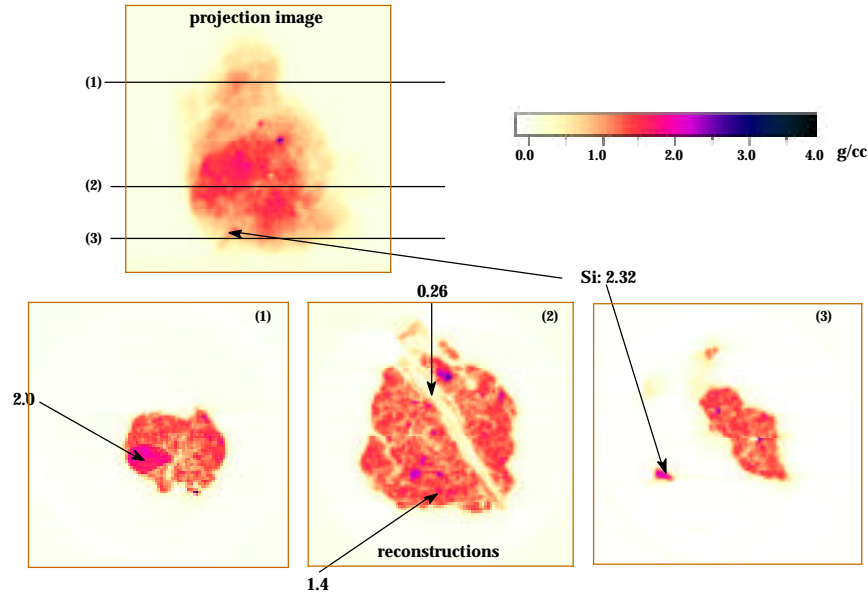


Fig. 5.38 Density map of a soil aggregate from an uncultivated field. The top figure is an absorption image of the sample as collected by the CCD camera. The bottom three images are reconstructed slices through the sample. In addition to the pores, a root canal with organic debris, a sandstone, and several heavy particulates are visible.

and dimensional stability, with graphite substrates as a potential lower cost alternative. Absorber patterns in 30-80 μm thick gold have been electroformed onto the beryllium after soft x-ray pattern transfer into 100 μm plus thick spun PMMA from a 2 μm conformal gold mask prepared by optical lithography. In collaboration with LaTech-IfM, we have tested prototype masks with graphite substrates and a 30 μm gold absorber. Preliminary results have encouraged us to incorporate graphite substrates into our mask technology.

We have also established gold electroforming capabilities as part of this program. These electroforming baths have been used in preparing some of the

prototype masks described above, and we have further improved the gold electroforming by working with Dover Industrial Chrome and vendors of the plating baths, resulting in different optimized baths for various applications. An example of this is shown in Fig. 5.39. We continue to work with Dover for the electroforming of nickel and copper structures and have commenced transferring the copper electroforming technology to the APS.

Employing the same gold-on-beryllium technology developed for mask fabrication, we have successfully fabricated for NASA a prototype x-ray coded aperture array. NASA tested the prototype for potential application in a gamma-ray telescope satellite, earning

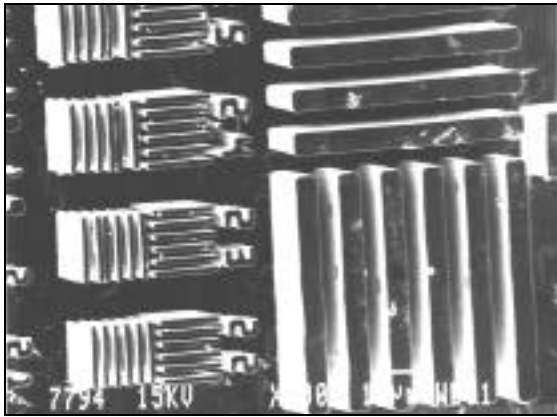


Fig. 5.39 Hard x-ray mask fabricated by XFD for DXRL with resolution test pattern showing features down to ~2 microns wide in 25-micron-tall gold on a 300-micron-thick silicon substrate.

an achievement award for our collaborator. Working with the RF group in ASD, we have fabricated prototype mm-wave RF accelerator structures suitable for RF testing. We have begun the fabrication of precision pinholes and slits for use at the APS. We have initiated collaborations with various groups in MSD at ANL in the area of material applications for micro-electromechanical systems (MEMS), as well as external collaborations with University of Chicago, University of Illinois at Chicago, Forschung Zentrum Karlsruhe (Germany), and KETI (South Korea).

We have completed a series of test exposures and development of 1-mm PMMA sheets under varying exposure conditions (mirror angles, scan speeds, dose rates) at 2-BM. These exposures have been used to determine the optimal exposure and development conditions, how to limit damage to PMMA during exposure, and methods for improved adhesion. As a result of these studies, we have optimized our standard processes to improve the

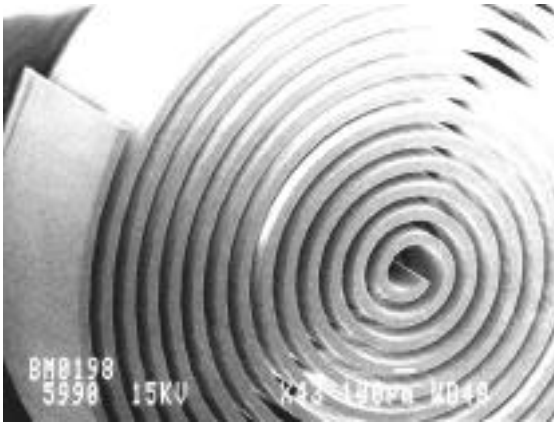
achievable resolution and depth attained using DXRL. Examples of this are shown in Fig. 5.40 (a) and (b). By successfully producing 1-6 mm thick PMMA structures on various substrates, we have also been able to demonstrate the advantages of using an APS bending magnet source for DXRL. These structures include 100 μm towers and holes and resolution test patterns for tests of development and adhesion. Aspect ratios of 100:1 have been achieved in a 2.5-mm-thick resist.

Finally, we have installed and commissioned a new precision x-ray scanner in the 2-BM-B station, and preliminary testing shows its capability to meet specifications. The scanner will be further enhanced by the addition of a rotational stage that will allow production of conicals and compound geometries.

2-ID-B Beamline and Optics

Most of the key optics and components of the 2-ID-B beamline were installed and commissioned by the end of 1997. Of major importance to the 2-ID-B scientific program is the successful commissioning and characterization of the 5.5-cm-period soft x-ray undulator, known as U5.5. To date we have operated it and commissioned the entirety of 2-ID (all three branch lines) at a minimum magnetic gap of 14.0 mm, corresponding to a fundamental energy of 635 eV and a maximum total power output of 7 kW. We have found that the 1.2-m-long M1 mirror (Si substrate, Si, Rh, and Pt stripes operating at 0.15° of incidence) in the 2-ID-A first optics enclosure performs exceptionally stably and reliably under the extreme power load of this source, the "hottest" undulator at the APS. Although we have yet to perform a precision absolute flux

(a)



(b)

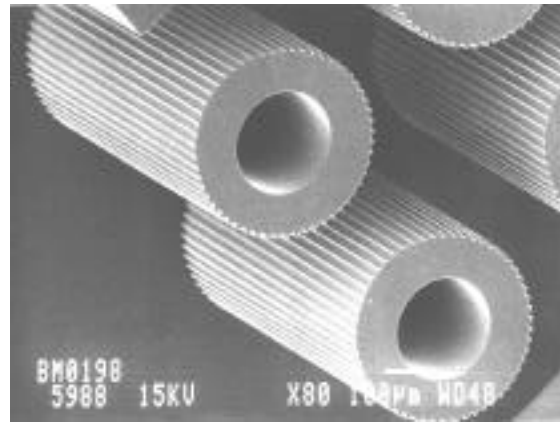


Fig. 5.40 1-mm-tall structures in PMMA reproduced using the hard x-rays from the APS and a gold-on-graphite x-ray mask fabricated as part of a collaboration between XFD, the Institute for Micromanufacturing at Louisiana Tech University (Ruston, LA), and Forschung Zentrum Karlsruhe (Germany).

measurement, the measured flux at the beamline end station is within an order of magnitude of that predicted using an Al vacuum photodiode. Moreover, by measuring the flux in the 120-nm diffraction-limited microfocus of a Fresnel zone plate with an avalanche photodiode, we have established that the coherent flux incident on the zone plate, and thus the source brilliance, is in the expected range.

The three soft x-ray pink beam position monitors (BPMs) were also installed and tested. By introducing small angular displacements in the x-ray beam with the M3B mirror, we determined that the spatial resolution of the BPMs is 1-2 μm , which is sufficient precision for closed-loop beam steering in combination with the M2B or M3B mirrors and for beam position monitoring. We have also completed much of the characterization and calibration of the 2-ID-B spherical grating monochromator (SGM), including measurement of a

resolving power $(E/\Delta E) > 3000$ at the Si 1s absorption edge using the 1800 gr/mm Pt-coated grating. The last optical elements to be installed in the 2-ID-B beamline, slated for late 1998, will be multilayer gratings, which are needed to access energies above ~ 2 keV.

High-Resolution Scanning X-ray Microscopy

Substantial progress has been made on the development of submicrometer scanning microscopy, microtomography, and microspectroscopy in the 1-2 keV energy region at 2-ID-B. The scanning x-ray microscope (SXM) uses a gold zone plate with a 100-nm-wide outermost zone to form an x-ray microfocus through which the sample is scanned. The measured efficiency of the zone plate at 1.57 keV is about 18%, within 2% of the theoretical value. Knife-edge scans through the zone plate focus

indicate the spatial resolution of the instrument is better than 150 nm (Fig. 5.41). The sample stage consists of a fast, two-axis electrostrictive actuator-driven fine stage with 6-nm resolution atop a stepper-driven coarse stage, and a precision rotational stage for orienting the sample at various angles of incidence to the zone plate focus. We characterized the performance of the SXM using pinhole and grid test samples. The fine stage motion is highly reproducible although

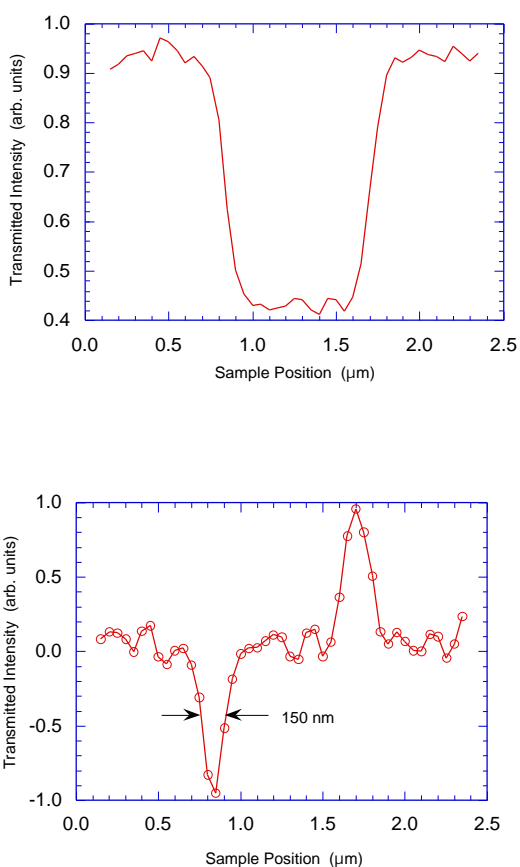


Fig. 5.41 (top) Knife-edge scan across an integrated circuit interconnect, and (bottom) its derivative showing the imaging resolution (focal spot size convolved with 50-nm scan steps and edge of the 500-nm-wide interconnect) is about 150 nm.

the scan field is somewhat warped; this is currently under investigation. The SXM currently operates in transmission mode using an avalanche photodiode (APD) as the transmitted flux detector. The plan is to deploy a low-energy Ge dispersive detector as a fluorescence detector in late 1998.

Scanning Microtomography and Microspectroscopy of Chips

As manufacturers of integrated microelectronic circuits (chips) seek to achieve higher component counts and densities, the feature sizes in these devices become correspondingly smaller. This and the higher current densities that may prevail pose additional constraints on the ability of such devices to tolerate electromigration effects as they age. Electromigration is the primary cause of unwanted transport of the materials used to carry electrical current in chips, leading to lattice strains, high-resistance conduction paths, and eventual failure. Consequently, a better understanding of electromigration is of tremendous importance to the microelectronics industry. Current means of imaging microelectronic devices, by visible light or by electron microscopy, are mostly limited to the sample surface, necessitating successive chemical or mechanical milling in order to investigate buried layers. Visible photons cannot resolve better than $\sim 0.25 \mu\text{m}$, electrons lead to sample charging, and neither probe is very sensitive to the sample constituents. X-rays in the few-keV energy range can penetrate the many layers in typical devices and uniquely offer elemental and chemical-specific contrast of the materials used to fabricate them (Al, Si, Ti, Cu, W, etc.). High-resolution 3-D x-ray microscopy therefore offers a better means to image the imbedded structures and buried

interfaces in chips without damaging them by thin sectioning. Moreover, the capability to perform element and chemical-state specific imaging at sub-micrometer resolution is highly attractive as a way to elucidate the detailed mechanisms behind electromigration processes in chips.

In collaboration with scientists from NIST, Rensselaer Polytechnic Institute, and Intel Corp., we are using the 2-ID-B SXM to image microelectronics devices in 3-D at 100-nm and smaller length scales in an effort to clarify the failure mechanisms due to electromigration effects. The samples we have explored to date, which were fabricated and backside-thinned to $\sim 10\ \mu\text{m}$ by Digital Equipment Corp. (DEC), consist of arrays of multilevel junctions of aluminum "interconnects" and tungsten "vias" embedded in an SiO_2 matrix. We used the SXM to record a series of high-resolution 2-D scanned projections through the samples at 6.92° angular increments over a 140° range of incidence angles. Each projection was $15\ \mu\text{m} \times 15\ \mu\text{m}$ in area and required about 30 min to acquire the 300×300 pixel scans with a dwell time of 10 ms/pixel. The projections taken at incidence angles above 60° from normal clearly show the 3-D nature of the sample features, especially the vias, which extend into the depth of the SiO_2 matrix. Tomographic reconstructions of the projection data set are underway, from which full 3-D views of the sample can be rendered. This technique, when fully developed, is promising for high-resolution 3-D chip inspection and defect analysis.

We also recorded normal incidence projections of the DEC samples over a range of incident photon energies. Figure 5.42 shows two scanned images of a pair of interconnect junctions, taken at two photon

energies on either side of the Al 1s absorption edge (Levine et al., 1998). These data demonstrate the capability of the SXM in combination with the SGM to obtain element-specific images at the 100-nm level.

Development of Soft X-ray XIFS

The other major experimental effort in the past year at 2-ID-B has focused on development of the tools and techniques necessary to mount and conduct soft x-ray speckle and intensity fluctuation spectroscopy (XIFS) experiments, in collaboration with scientists from ANL MSD and Massachusetts Institute of Technology (MIT). XIFS shows promise for investigation of fluctuations in disordered samples near phase transitions, both at and far from equilibrium. In particular, 1-4 keV x-rays are suited to probing materials composed of the low-Z elements, such as biological objects and polymers. In this work so far we have prepared a highly coherent x-ray beam and used it to record Fraunhofer diffraction patterns with monochromatic and with pink beam (Fig. 5.43), and static speckle patterns produced by a silica aerogel sample. We have used both a $10\text{-}\mu\text{m}$ -diameter pinhole and a zone plate to define a $\sim 10\text{-}\mu\text{m}$ -diameter and a $\sim 250\text{-nm}$ -diameter coherent illumination spot on the sample, respectively. The sample itself was mounted on a $5\text{-}\mu\text{m}$ - or $15\text{-}\mu\text{m}$ -diameter pinhole, respectively, to block parasitic scattering from previous apertures in the beam. The speckle patterns were recorded initially by a scanning pinhole and the APD; we now use a CCD camera in direct-detection mode for its greater speed and simplicity of use. With the CCD camera, we have learned that use of a zone plate to increase the flux density

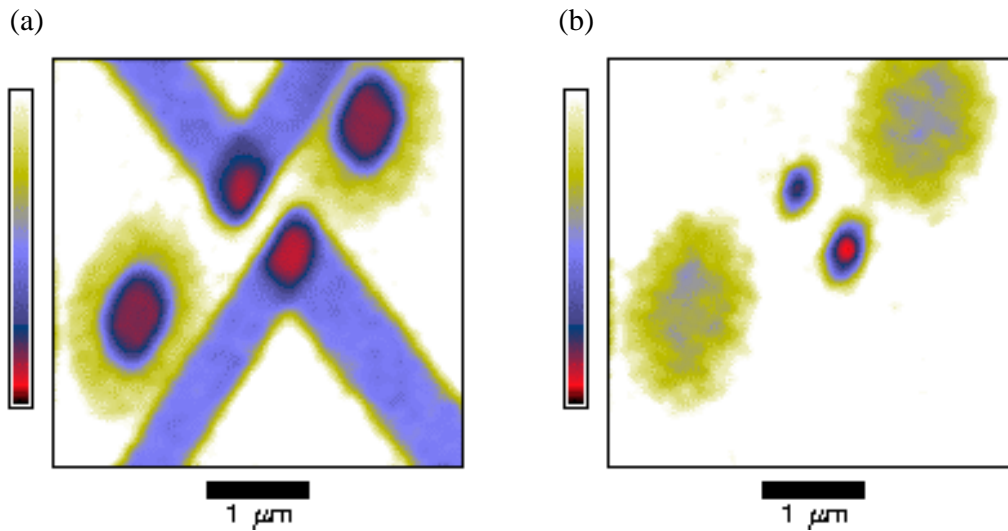


Fig. 5.42 Images of two Al/W integrated circuit interconnect junctions taken at (a) 1563 eV and (b) 1553 eV. The aluminum interconnects forming the junctions become nearly transparent on the low-energy side of the Al 1s absorption edge (1559 eV), whereas the small tungsten via joining the interconnects still appears dense. White and red indicate high and low transmission, respectively.

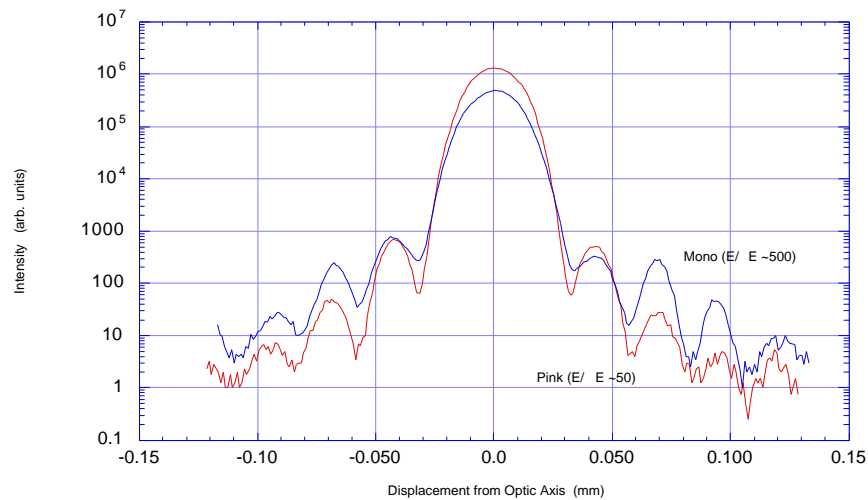


Fig. 5.43 Fraunhofer diffraction pattern of a 5- μm pinhole recorded with coherent 1793-eV x-rays, using both monochromatic and pink beam at a distance of 217 mm.

on the sample and to enlarge and simplify the speckle pattern is advantageous. It also allows for a shorter working distance so that speckles at higher momentum transfer can be observed. Furthermore, the speckle size can be matched to the detector geometry by adjusting the position of the sample with respect to the microfocal plane. Lastly, we showed that the speckle contrast increases for energies just above the absorption edge for major elemental constituents in the sample, in this case, above the Si 1s edge in the aerogel. Figures 5.44 (a) and (b) show speckle patterns recorded with the CCD camera in the pinhole and zone plate setups, respectively.

2-ID-C Beamline and Optics

The soft x-ray polarization and spectroscopy (XPS) beamline, 2-ID-C, is the last branch line of 2-ID to be constructed. As a result the 2-ID-C beamline is still under

commissioning and final alignment status. However, the past year has seen great progress towards declaring the 2-ID-C beamline operational. All major components as far as the first diagnostic end station have been tested, integrated into the EPICS control system, and subjected to initial measurements and characterization. In particular, the M2C horizontal focusing mirror, M3C vertical focusing mirror, high-heat-load entrance slit, exit slit, and two of the gratings (600 grooves/mm and 1200 grooves/mm) for the 2-ID-C beamline have been commissioned and aligned down to the current minimum allowable gap (14.0 mm) of the U5.5 undulator.

We have made preliminary x-ray absorption measurements utilizing the diagnostic end station. Figure 5.45 shows the x-ray absorption spectrum at the Gd 3d 5/2 absorption edge of gadolinium oxysulphide. The measured resolving power of ~6000 approaches the predicted theoretical

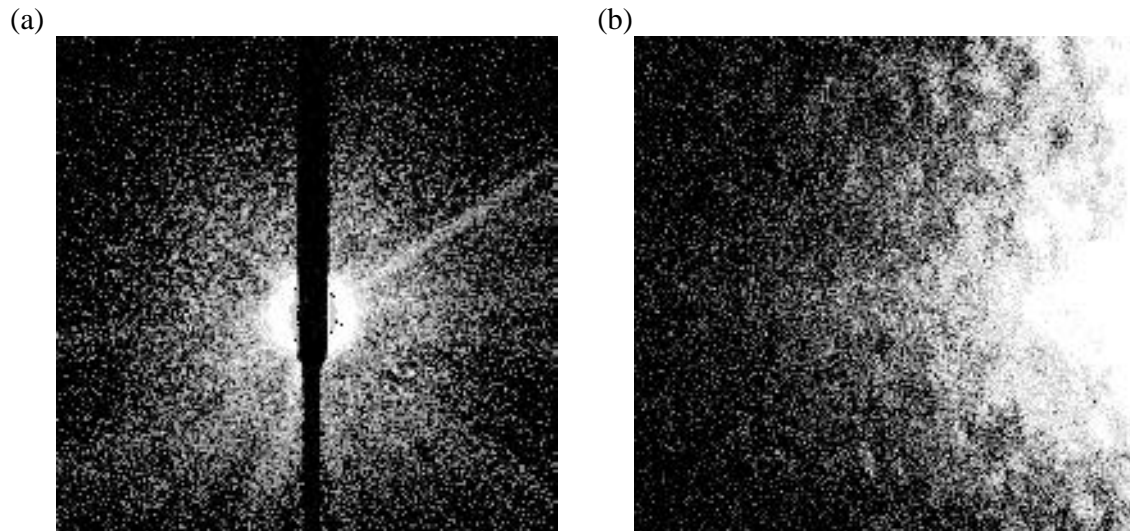


Fig. 5.44 High contrast speckle patterns recorded with (a) a pinhole setup and (b) a zone plate setup.

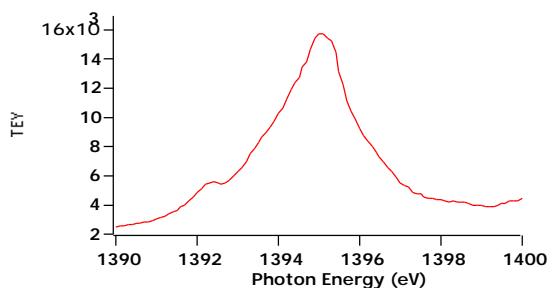


Fig. 5.45 X-ray total electron yield (TEY) spectrum of gadolinium oxysulphide recorded at the Gd 3d 5/2 absorption edge with 20- μm slits on the 2-ID-C beamline.

performance of the SGM. Estimation of the resolving power utilizing x-ray absorption data is difficult at these resolving powers as the resolution approaches the natural line width. Future development of the XPS end station will allow for more accurate resolving power determination by looking at narrow core lines and Fermi levels.

The development of the XPS end station and a x-ray fluorescence end station will continue in parallel with the final commissioning and alignment of the beamline. The plans call for development of productive programs in x-ray absorption, x-ray emission, and x-ray photoelectron spectroscopies in the 0.5-3.0 keV energy range, with a particular emphasis upon the lanthanide series.

2-ID-D/E Beamline and Optics

The 2-ID-D/E branch line was also completed by the end of 1997. Most of our construction efforts since then have been devoted to development of the 2-ID-E and 2-ID-D end stations, commissioning of new detectors and scan systems, and refinement

of the experimental apparatus. In the area of microfocusing optics, the performance of the Fresnel zone plate was significantly enhanced in three areas: (1) higher spatial resolution, (2) higher focusing efficiency, and (3) extension to higher energies.

Our principal achievement was to demonstrate for the first time in the hard x-ray spectral region that Fresnel zone plates are capable of focusing a x-ray beam to a submicrometer spot size with a flux density gain at the focus of more than four orders of magnitude. We obtained a full-width-half-maximum (FWHM) focal spot size of 150 nm at the first-order focus of a zone plate with a 100-nm outermost zone width (Fig. 5.46). For a partially coherent beam (no source aperturing), this represents a very high gain of 3×10^4 in the x-ray flux density at the focus compared to the incident beam. If the beam is fully coherent, by aperturing the source size, the gain can be further increased to a record 1.2×10^5 . This is probably the highest flux density gain reported for any microfocusing x-ray optic, and high spatial resolution with high gain is essential for many applications of x-ray microprobes. For instance, our recent measurements on imaging trace elements in bacteria were made possible only with the availability of these high-resolution optics. On the same zone plate, we also demonstrated a FWHM focal spot size less than 90 nm using the third-order focus.

Another important performance criterion of microfocusing optics is their efficiency. We have made important progress in improving the diffraction efficiency of x-ray zone plates by using a blazed zone profile. Although an ideal phase zone plate with rectangular zone profile has a first-order diffraction efficiency of 40%, a significant fraction (at least 60%) of the incident

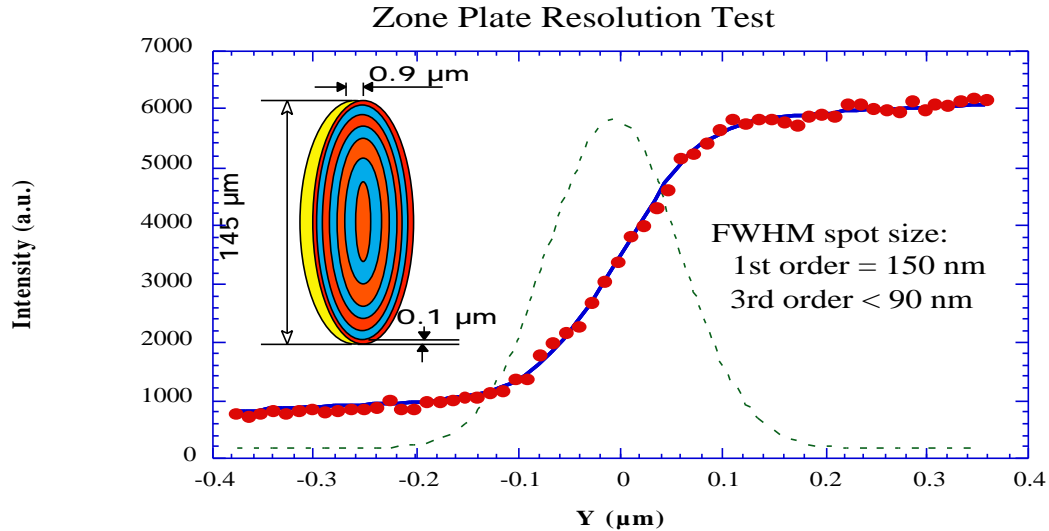


Fig. 5.46 Fluorescence intensity (red dots) from a Cr knife-edge as it was scanned through the focus of a high-resolution zone plate. An error function (green dotted line) with 150 nm FWHM was integrated and fitted to the fluorescence data (blue solid line).

photons are delivered into the other diffraction orders. Instead, by blazing the zone profile (approximated in this case by a staircase with as little as four steps), we demonstrated focusing efficiencies of 39% and 45% with a circular and a linear Fresnel zone plate (Fig. 5.47), respectively, surpassing the 40% limit of a conventional phase zone plate with rectangular zone profile. More importantly, as more x-rays are delivered to the first-order focus, fewer photons end up in the unwanted orders. The result is a much higher peak-to-background ratio. On the zone plate with stepped profile, the measured flux density of the focused spot is 3.6×10^3 times higher than the background. Not only is this beneficial for imaging and coherence applications, it also allows the implementation of large sample environmental chambers by removing the need of an order-sorting aperture close to the sample.

Most of the zone plates developed so far were optimized for the 8-20 keV energy range. Although there is great interest in using zone plates for high-energy applications (20-100 keV), the fabrication process becomes increasingly challenging as larger thicknesses are required to maintain a phase shift at higher energies. An alternative is to stack multiple zone plates, with a common optical axis, for high-energy use. This not only increases the capabilities of currently available zone plates by several fold, it also opens up a new realm of microfocusing applications in the high-energy regime. In an experiment performed at 1-ID-C (which has high x-ray energy capabilities), we showed that stacking and aligning two zone plates with an individual efficiency of 13% when used separately yields a combined efficiency of 25% at 40 keV, which is as good as the efficiency we normally obtained for most zone plates at lower energies (8-20 keV). More

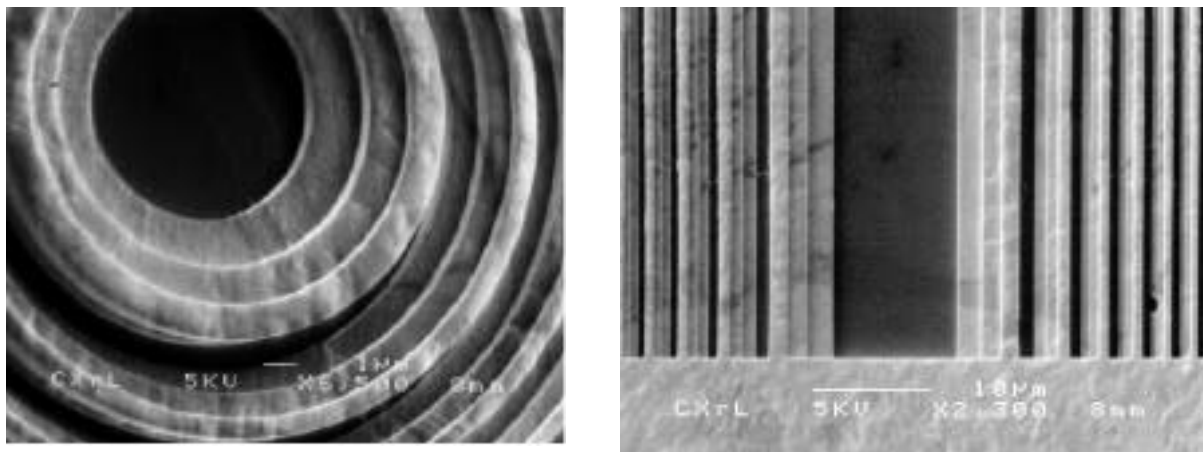


Fig. 5.47 Scanning electron micrograph of a circular (left) and a linear (right) zone plate with a staircase-like blazed zone profile.

importantly, this shows that by aligning multiple zone plates together it will be possible to use zone plates for much higher energies than was possible previously.

X-ray Microfocusing Applications

The development of microfocusing-based techniques is directly coupled to its applications. X-ray fluorescence microscopy (XFM), microdiffraction (XMD), microspectroscopy, microbeam small-angle scattering (XMSAS), fluorescence correlation spectroscopy (XFCS), and x-ray fluorescence tomography (XFT) have been developed and demonstrated in a series of experiments at the 2-ID-D station. These techniques have been applied to the following applications: (1) study of dynamics of colloidal systems using XFCS in collaboration with a scientist from Northern Illinois University and ANL MSD; (2) anticancer agents in collaboration with scientists from La Trobe University and the University of Melbourne (both in Australia); (3) trace elements distribution in SiC nuclear

fuel shell using XFT in collaboration with scientists from Oak Ridge National Laboratory; (4) local molecular alignment within mesoscopic fibers of DNA-cationic membrane complexes using XMSAS in collaboration with scientists from the University of California, Santa Barbara; (5) study of an electro-absorption laser/modulator using XMD in collaboration with scientists from Lucent Technologies; (6) study of the plant-fungi relationship in contaminated environments using XFM in collaboration with scientists from ANL ER; (7) mapping of strain field and crystallographic phases near the edge of a ground steel component using XMD in collaboration with a scientist from Warner Lambert, Inc.; (8) electromigration study using XMD in collaboration with scientists from the University of Wisconsin; (9) study of functions of Cu in cells using XFM in collaboration with a scientist from MIT; (10) imaging of trace elements in bacteria using XFM in collaboration with scientists from ANL ER; (11) strain field mapping by XMD near a crack tip and measurement of single grains within a finite size specimen in collaboration with a scientist from Los

Alamos National Laboratory; and (12) source identification of airborne pollutant particles using XFM in collaboration with a scientist from the Australian National Science and Technology Office. A brief description of some of these applications is provided in the following.

X-ray Fluorescence Correlation Spectroscopy

Photon correlation spectroscopy, which is used to study the dynamics of particles in fluids by measuring the fluctuations in the scattered and fluorescent intensity, is a well-established technique with visible light. With the advent of high-brilliance synchrotron radiation sources, such techniques have recently been extended to the x-ray wavelength region by utilizing x-ray beams possessing a high degree of spatial coherence and by studying the time fluctuations of the corresponding speckle patterns from the samples in question. In this present study, we have developed a related technique, x-ray fluorescence correlation spectroscopy (XFCS), for elucidating the dynamics of single particles or clusters of particles (Wang, 1998). This method relies on an intense microfocused x-ray beam but does not require a coherent beam per se. A distinct advantage of this method is elemental specificity by using an energy-dispersive x-ray detector. This method is particularly useful for studying both diffusive particle motion and flow in optically opaque systems for which methods employing visible light are not suited. As a demonstration of the method, the dynamics of gold and ferromagnetic colloidal particles and aggregates undergoing both diffusion and sedimentation in water have been studied by measuring the time-autocorrelation of the x-ray fluorescence

intensity from a small illuminated volume (Fig. 5.48). The dynamic parameters obtained are in excellent agreement with theoretical estimates and other measurements. This technique has recently been used to study the dynamics of red blood cells (RBC) in whole human blood, also shown in Fig. 5.48, as well as the thermal stability of RBCs and the interaction between the RBCs and foreign ions. In addition, we have demonstrated that the microfocused beam size and incidental effects of instrumental vibration can be determined independently and precisely by XFCS. The potential applications of XFCS include the study of the motion of biological macromolecules containing heavy atoms on or across membranes; the study of interdiffusion of atoms at interfaces between two species of materials; the study of the sedimentation or flow of colloidal particles in fluids containing polymers or surfactants which, we note, is unobservable by coherent x-ray intensity fluctuation spectroscopy techniques.

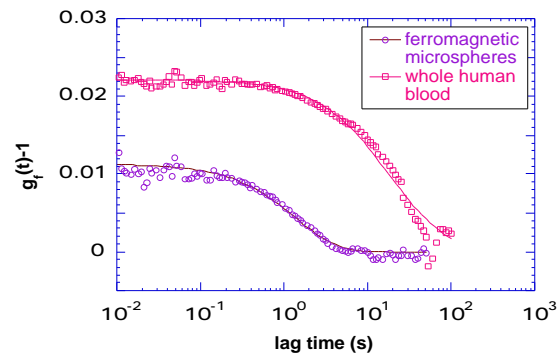


Fig. 5.48 Time autocorrelation functions obtained from the Fe K fluorescence emission from two samples: ferro-magnetic microspheres, and red blood cells in whole human blood. The solid lines are the fits utilizing models describing both diffusion and sedimentation motions.

X-ray Imaging Studies of the Mycorrhizal Fungus-Plant Symbiosis

Approximately 90% of the world's vascular plants, including the majority of all economic crops, belong to families that commonly have symbiotic associations with mycorrhizal fungi. While such associations are known to increase plant viability under low nutrient conditions, in some instances mycorrhizal fungi can also moderate toxicity effects in plants growing on soils containing elevated concentrations of heavy metals. Thus, an improved understanding of the plant-fungus relationship, particularly with respect to the uptake and regulation mechanisms for metals and micronutrients, is expected to have significant implications in both agriculture and the remediation and restoration of contaminated environments.

We have applied x-ray fluorescence microscopy to study the symbiotic relationship of *Plantago lanceolata* L. roots

that have been infected by the arbuscular mycorrhizal fungus *Glomus mosseae*. The roots were kept in their natural hydrated state without any staining, thus avoiding any artifact due to sample preparation. The distributions of micronutrients Mn, Fe, Cu, and Zn were recorded simultaneously with those of P, S, K, Ca, and Ni, using a microfocused x-ray beam of $1\ \mu\text{m} \times 3\ \mu\text{m}$. The elemental sensitivity is approximately 500 ppb, considerably better than that of either electron or proton microprobes. Typically, the fungal hyphae can be distinguished from root hairs because they branch and enter the root at multiple points. We found low concentration of Mn in the fungal hyphae, which agrees with the fact that mycorrhizal plants tend to have much less Mn than non-mycorrhizal plants. Also, the results (Fig. 5.49) indicate that Fe tends to be most concentrated on the edge of the root, perhaps reflecting the precipitation of Fe in this location. Zn seems to typically show up most strongly in the fungal hyphae and in the center of the root, most likely in the inner cortex where the proliferation of

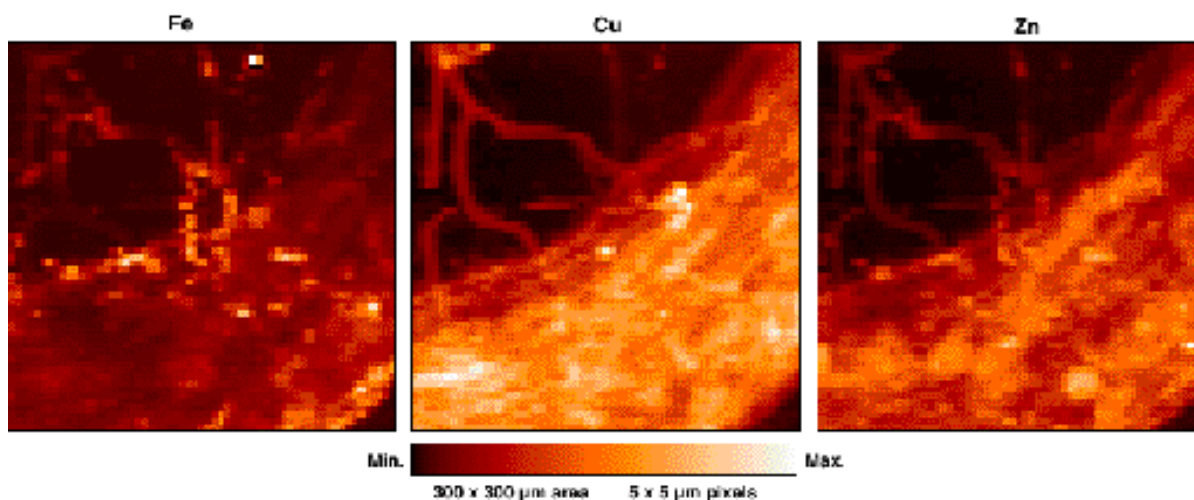


Fig. 5.49 Elemental distribution of Fe, Cu, and Zn in a plant root infected by mycorrhizal fungus. The scan area is $300\ \mu\text{m} \times 300\ \mu\text{m}$, with $5\text{-}\mu\text{m}$ steps in both directions.

the fungus is typically the greatest. This suggests the use of Zn as a surrogate measure of mycorrhizal fungi in roots and additional work is underway to confirm this correlation. In addition, we recorded micro-XANES spectra of the Mn K-edge at selected positions within the hydrated sample, including on a single fungal hypha, to study the chemical state. Ninety percent of the Mn sampled by the x-ray beam is in the Mn^{+2} state, the soluble and most useful form to plants and fungi. This experiment clearly demonstrates that the microprobe is capable of providing high-quality micro-XANES measurement with micrometer-scale resolution.

Detection of Platinum Anticancer Agents in Ovarian Cancer Cells

Cisplatin is one of the best anticancer agents for the treatment of testicular cancer, and is also used for a wide range of other tumors (e.g., ovarian, head and neck, lung). Cisplatin has a variety of dose-limiting side effects, including nephrotoxicity and neurotoxicity. Its analogue carboplatin has fewer severe side effects and is also in widespread use for treatment of similar tumor types. One of the major reasons for failure of a tumor to respond, or for a tumor to relapse when treated with cisplatin and carboplatin, is the presence of intrinsic (inherent) or acquired resistance, which was developed when the cancer was treated with cisplatin. If a cisplatin analogue was able to overcome this platinum resistance, cancer therapy could be substantially improved. There has been considerable interest to find derivatives of cisplatin that exhibit good activity against cisplatin-resistant cells. The development of these derivatives has been severely hampered by the lack of a clear understanding of the molecular processes

involved in the development of this resistance, partially due to the lack of a tool that would allow one to quickly measure the interaction of the cisplatin or carboplatin derivatives with the cisplatin-resistant cells. Several resistance mechanisms have been identified in cisplatin-resistant cells in laboratory studies, including increased levels of cytosolic detoxifying, such as glutathione and metallothionein, enhanced repair of DNA damage, tolerance of cells to DNA damage, and decreased cellular or nuclear accumulation. However, it is not known which mechanism is the most important clinically. It is likely that a major advance in understanding this phenomenon can be gained by ascertaining how the subcellular distribution of cisplatin derivatives changes between resistant and sensitive cells.

The x-ray microprobe at 2-ID-D was employed to map the spatial distribution of cisplatin and its derivatives in the resistant and sensitive cells using platinum M-line fluorescence. The platinum derivative used in this study is a drug known as Pt103. It has been selected as the lead compound for development of future compounds based on its good activity against platinum-resistant cell lines. Normal ovarian cancer cells 2008 and cisplatin-resistant cells C13 were treated with cisplatin and Pt103, respectively, for varied time periods for comparison of the effectiveness between anticancer agents, between sensitive and resistant cells, and among different treatment times.

The x-ray beam was tuned to 11.7 keV and was focused by a zone plate of 10-cm focal length to a spot size of $0.2 \mu m \times 0.5 \mu m$. Figure 5.50 shows a platinum fluorescence image of a sectioned ($1 \mu m$ thick) cell treated with agent. The platinum distribution

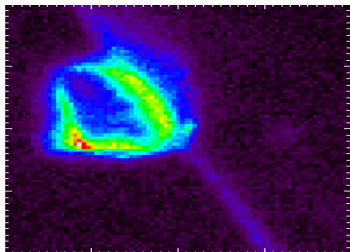


Fig. 5.50 Elemental distribution of Pt agent measured on a thin section ($1\ \mu\text{m}$ thick) of an ovarian cancer cell. The Pt distribution is very localized. The scan area was $40\ \mu\text{m} \times 40\ \mu\text{m}$.

is highly localized, which can provide insights into understanding the reaction of the cancer cells to the agent at a subcellular level. In addition, we measured the fluorescence signals obtained from individual whole cells, thereby studying the efficiencies of cisplatin and Pt103 to 2008 and C13 cells under different treatment times. The results show that the Pt103 derivative is five times more effective than cisplatin in platinum-resistant cells and is three times more effective in normal 2008 cancer cells after treatment for 8 and 24 hours. The effectiveness of both agents in 2008 and C13 cells increased as treatment time increased. For most of the cisplatin samples scanned, there was a more pronounced nuclear localization than for Pt103, which showed a more homogeneous distribution. The level of platinum sensitivity was several orders of magnitude higher than previous results obtained with the proton microprobe PIXE. This shows that a x-ray microprobe can provide a new tool for studying uptake of chemical agents at the cellular and subcellular levels.

Measurement of Strain Field and Crystallographic Phases at the Edges of Steel Components

The surface hardness and fatigue resistance of the edges of a ground component made of martensitic stainless steel are a function of the amount of retained austenite, its residual stress, and its carbide parameters. The cold work induced by grinding causes a phase transformation from austenite to martensite, which is associated with a volume expansion and increased residual compressive stress. The residual stress at the ground surface of such components has not been measured successfully before because of the large beam size of conventional x-ray diffraction sources. In order to optimize the performance of these components, it is essential to establish a method to measure the residual stress at the ground surface on micrometer length-scales, and to understand how the residual stress changes are related to the grinding process.

At beamline 2-ID-D/E, we used an x-ray microdiffraction technique to characterize the lattice strain distribution in thin martensitic stainless steel components as a function of their grinding parameters. The lattice strain of the samples was determined from CCD camera images of the x-ray microdiffraction pattern resulting from the martensite (110) and austenite (111) planes. Micrometer-size ($0.5\ \mu\text{m} \times 3\ \mu\text{m}$) areas near the edges of the samples were illuminated with a 12-keV x-ray microbeam formed with a zone plate lens. The samples were aligned such that the scattering vector was

along their edges. The lattice strain of the martensite (110) plane was measured as a function of the distance from the illuminated area to the sample edge. During each CCD exposure of the sample diffraction pattern, at a given distance from its edge, the sample was scanned along the horizontal direction to enhance the statistics of the measurement.

Figure 5.51 shows two CCD images of the diffraction patterns near the edge of one sample. The pattern obtained 40 μm from the edge shows diffraction from phases of both austenite and martensite. Only diffraction from martensite phase was observed 1 μm from the edge, indicating that a phase transformation from austenite to martensite took place during the grinding process. We also observed a smaller lattice

constant along and near to the edge, suggesting a compressive residual stress resulted from the phase transformation. We performed x-ray microdiffraction measurements at distances of 1-600 μm from the edges of several samples containing 12% and 20% initial retained austenite to correlate the amount of retained austenite to the residual stress after grinding. The results indicate that the samples with a higher (20%) retained austenite not only had a higher residual compressive stress than the ones with lower (12%) retained austenite, but also had a higher retained austenite after grinding. In the future we hope to determine the optimum residual stress and retained austenite combination to maximize the hardness and fatigue resistance of the ground surface of such components.

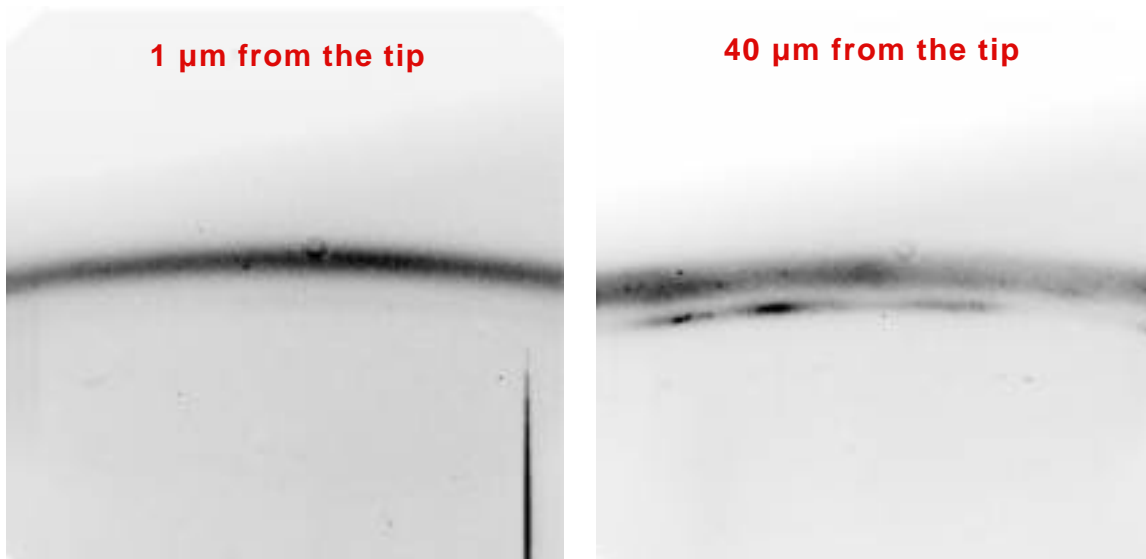


Fig. 5.51 Microdiffraction patterns taken at the tip of a thin stainless steel component.

Strain Measurement on a Single Grain Using Microdiffraction

An understanding of fracture mechanisms is important in evaluating the aging of materials. Conventionally, neutrons and x-rays have been utilized to map the residual stress/strain, mosaicity and crystallite size, etc., but they were limited to bigger gauge volumes. We developed a new method to examine much smaller gauge volumes (10^{-3} to 10^{-5} mm³) and with higher spatial resolution (1 μ m) unlike the neutron measurements. These new results could lead to doing crystallography on single grains and will help to understand micro-stresses and strains in materials.

The microdiffraction measurements were carried out on beryllium Compact Tension (CT) specimens of differing textures in the critical region (i.e., in and around the notch point) at room temperature by using 11.0-keV x-rays at 2-ID-D beamline. The Be sample with a load cell is mounted on a stage that has translational and rotational manipulation. The load is changed manually, and then the beam is aligned at the notch with a x-ray phase contrast image. A CCD detector is used to record the diffraction pattern from the sample. The diffraction peak from each individual grain can be tracked when the load is changed. Such a case is shown in Fig. 5.52, where the diffraction peak position (along the azimuthal direction) is plotted for

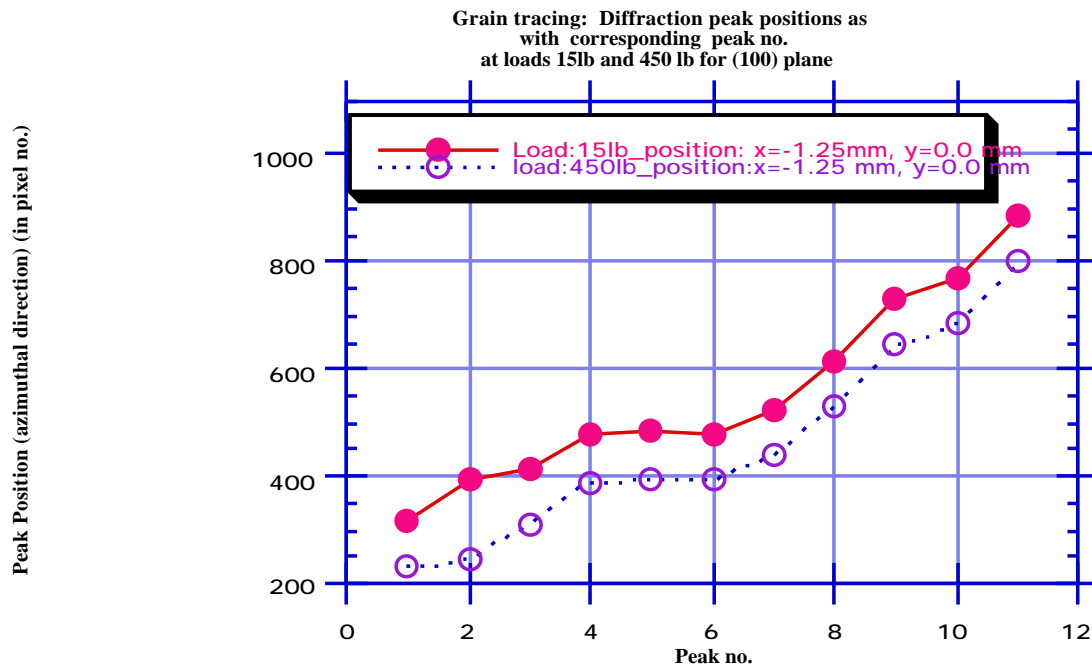


Fig. 5.52 The azimuthal locations of 11 diffraction spots recorded with the CCD camera under loads of 6.8 and 205 kg. The fact that the two curves have the same shape suggests that the same 11 grains were diffracting under both loading conditions.

11 diffraction spots when the load was increased from 6.8 to 205 kg. The fact that the relative peak position does not change indicates that the same grain is diffracting in both cases, allowing us to track the strain of individual grains during the stress measurement, which will provide valuable data previously unavailable for simulation and finite element calculation. The result shows that the microstrain increases at the notch point for the Be (100) reflection. At 1 mm away from the notch, the microstrain did not recover fully but is smaller than that at the notch. We also determined that the mosaic spread increases at the notch point and is large with larger load

5.4.4 Sector 3

Developments at the 3-ID Beamline

During the past year, the remaining two stations of the 3-ID beamline were completed. Stations 3-ID-C and 3-ID-D became operational in February 1998, opening the way for independent investigators by February 1999. During the year, there were some important upgrades to the beamline including the installation of a 5-mm internal gap ID vacuum chamber, which allows us to have the undulator between 6-30 keV with no spectral gap. Beamline 3-ID became the first in which the undulator gap can be reduced to 8.5 mm (see section 5.1.5 for details). Additional shielding to the white beam shutter and FOE has been completed, and the undulator gap can now be reduced to its minimum value of 8.5 mm. Another important change was the installation of diamonds as high-heat-load monochromator crystals. Studies conducted at an undulator gap of 8.5 mm indicated no adverse affects on beam divergence. This

water-cooled system has been in place since May 1997, and the first year of experience is satisfactory.

During the year, we also commissioned the collimating and focusing double-groove mirror and demonstrated that the beam divergence can be reduced from $17 \times 40 \mu\text{rad}$ (vertical and horizontal) to $11 \times 20 \mu\text{rad}$. When testing, the reflectivity of the mirror is better than 97% in the 7-24 keV range. The focal spot size in the 3-ID-C station has been measured to be less than $450 \mu\text{m}$ horizontal and $300 \mu\text{m}$ vertical after the high-energy-resolution monochromator.

The general approach followed when conducting high-energy-resolution experimentation at beamline 3-ID was to unify the monochromatization process and develop different styles of analyzers. The inelastic x-ray scattering setup using an "in-line" monochromator and curved crystal backscattering is shown in Fig. 5.53 (a), and the configuration for inelastic nuclear resonant scattering is shown in Fig. 5.53 (b).

The underlying principle in high-energy-resolution monochromatization is to employ an optimum combination of asymmetrically cut single-crystal reflections to create the desired energy bandpass, angular acceptance, and overall efficiency or throughput. Several different software packages have been developed to optimize certain parameters, such as the choice of reflection planes, the degree of asymmetry, and energy resolution (Toellner, 1996). These programs include calculation of modified DuMond diagrams (Mooney, 1990); accurate 3-D (angle-energy-reflectivity) throughput calculations of multiple-crystal systems, including the source divergence and bandpass (Toellner, 1998); and the complete treatment of

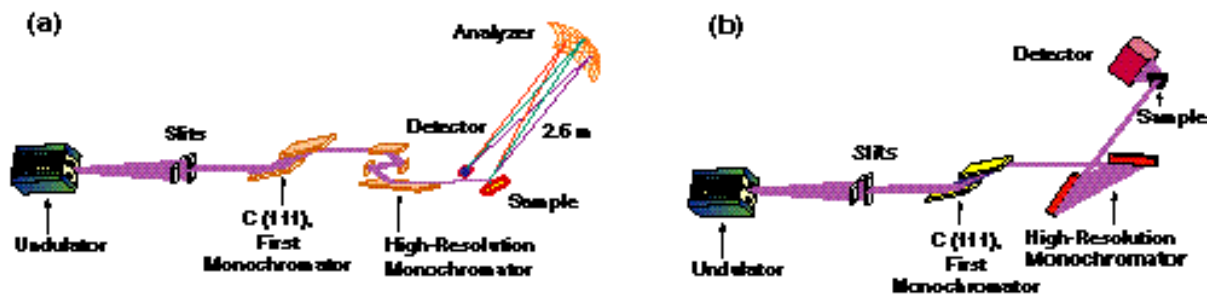


Fig. 5.53 The schematic layout for high-energy-resolution inelastic x-ray scattering as implemented at the 3-ID beamline of SRI-CAT. (a) The inelastic x-ray spectrometer that consists of an “in-line,” nested, 2-channel-cut design high-resolution monochromator followed by a curved crystal analyzer. (b) The inelastic nuclear resonant scattering spectrometer that consists of two flat-crystal monochromators followed by a fast detector with nanosecond resolution for time discrimination. An in-line monochromator, as shown in (a), is also available for several isotopes for coherent or incoherent nuclear resonant scattering.

multibeam excitations in single crystals, including exact backscattering (Colella, 1998).

As for new monochromator components, we have completed a 1-meV-resolution silicon monochromator at 21.5 keV, and 3.4-meV-resolution monochromator at 24 keV, and a 2-meV, 0.8-meV, and 0.6-meV resolution monochromator at 14.4 keV. It is worthwhile to note that the energy bandpass of the 0.66-meV-resolution monochromator at 14.413 keV with 3×10^8 photons/sec represents the highest photon flux with the lowest E/E achieved so far, using the flat-crystal concept described previously (Toellner, 1996; Toellner et al., 1997; Chumakov et al., 1996a). The monochromators at 21.5 and 14.4 keV can be used both for inelastic x-ray scattering with a backscattering analyzer and for nuclear resonant scattering purposes.

Analysis of the energy spectrum of inelastically scattered x-rays with sufficient resolution and efficiency continues to be a challenge. The conflicting aspects of this

method stem from the divergent nature of the scattered x-rays and the limited angular acceptance of crystals used as analyzers. The problem becomes particularly serious when the required resolution drops below 10 meV in the 6-30 keV range. The established method, originally introduced in the early 1980s (Dorner et al., 1986), involves the use of near-backscattering geometry from high-order Bragg reflections. In order to improve the total solid angle subtended by the analyzer, the thin crystal would be bent to a spherical shape with several-meters radius of curvature. This, accompanied by several different procedures to reduce or eliminate bending stress (Burkel et al., 1989; Verbeni et al., 1996), provides a reasonable solution to an immediate problem. We have developed a new procedure for use in preparing 10-cm-diameter diced analyzers comprising approximately 8,000 crystals. With respect to earlier methods, we take a new approach to reducing the strain on the curved analyzer. A Pyrex wafer was used as substrate to position the 8,000 crystals. Then, the Pyrex-epoxy-silicon “sandwich” is pressed into a concave substrate with a

2.6-m bending radius (Schwoerer-Böhning et al., 1997).

Resonant and Non-Resonant Inelastic Scattering Program

Inelastic x-ray scattering is a powerful and important tool for the study of collective excitations in condensed matter systems. The technique measures the dynamic structure factor, which leads to an understanding of electron or atomic correlations in space and time. At moderate energy resolutions (few hundred meV), electron correlations can be studied in metallic systems, strongly correlated electron systems, etc.

At ultrahigh energy resolution (a few μeV to meV), the dynamic correlations of ion cores (phonons) can be studied using the inelastic x-ray scattering technique in systems where traditional methods, such as neutron scattering, may be less applicable. These include ultrahigh-resolution nuclear x-ray inelastic scattering to derive partial phonon density of states from disordered systems, thin films, nano-particles, etc. The ultrahigh-energy-resolution x-ray experiments will also focus on the dynamics in glasses and liquids.

The use of backscattering geometry provides an opportunity to measure phonon frequency-momentum dispersion relations along high-symmetry crystallographic directions from single-crystal samples. The inelastic spectrometer in the 3-ID-C station has been used to measure spatial phonon dispersion in diamond with an overall instrument resolution of 9.2 meV. Diamond has unusual static properties when compared to other class IV tetrahedral semiconductors.

Lattice dynamical characteristics, such as phonon dispersion and thermal expansion, are also distinctive. Additionally, the occurrence of the most energetic phonons away from the Brillouin zone center is peculiar to diamond. A necessary condition to have such an overbending is to have sufficiently large second-nearest-neighbor force constants. Figure 5.54 shows an example of a phonon dispersion in diamond measured along the [111] direction, the complete set of dispersion data is shown in Fig. 5.55. The expected overbending in the most energetic LO branch along both Γ -X (Γ -L) and Γ -K (Γ -L) and the elliptically polarized Σ branch along Γ -K (Γ -L) received special attention in our measurements. Overbending in all three directions has been invoked to explain an extraordinary peak in the two-Raman spectrum. The overbending from our measurements is seen only along Γ -X (Γ -L) (Schwoerer-Böhning et al., 1998).

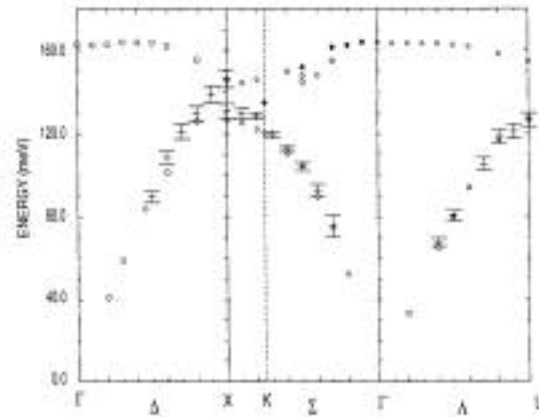


Fig. 5.54 Longitudinal phonon branches along Γ -X, Γ -L, and Γ -K. Symbols without error bars are high-resolution inelastic x-ray scattering data; symbols with error bars were obtained by inelastic neutron scattering.

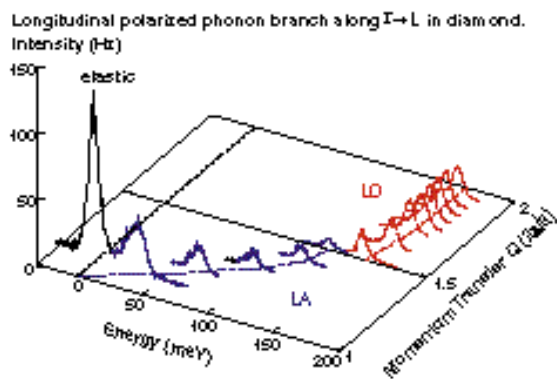


Fig. 5.55 Spectra at different momentum transfers representing longitudinal acoustic and optic modes in diamond along the $[111]$ direction (L). The measurements were carried out using the Si (777) reflection of the analyzer at a Bragg angle of 89.97° with a total energy resolution of 7.5 meV. These data prove that there is no measurable overbending in the optical mode as predicted by *ab initio* calculations.

Resonant inelastic scattering from insulating cuprates with 0.8-eV resolution was demonstrated, and the high flux was used to acquire systematic data, which were essential for understanding the nature of the resonance process. Also, the energies of various electronic states near the Fermi surface were measured. Given the experimental challenges in achieving the high energy resolution required to measure exciton dispersion, we instead used the fact that the coupling mechanism between the electronic charge and photons is highly polarization dependent to deduce information on the symmetry of the high-energy excitations we had seen earlier. This involved measuring the detailed resonance profiles for a variety of experimental geometries using (001), (100) and (110) cut $\text{Sr}_2\text{CuO}_2\text{Cl}_2$ single crystals. It was possible to deduce that the high-energy transitions we had seen are highly polarized in the b_{1g}

(i.e., $d_{x^2-y^2}$) channel and probably correspond to transitions from the b_{1g} ground state to a broad a_{1g} continuum that comes from an antibonding combination of the Cu $3d_{x^2-y^2}$ orbital and the surrounding O $p(s)$ orbitals. Complete assessment of these measurements is underway.

Figure 5.56 demonstrates the capability for studying phonons in transition metals. To study electronic energy levels near the Fermi level, a backscattering Ge analyzer with 100-meV resolution at 9 keV has been tested with direct incident beam of 700-meV bandpass. This spectrometer has been used to study correlated electron systems in rare-earth cuprates.

The inelastic scattering technique described above requires the use of single crystals. In order to study polycrystalline materials, powder samples, and, in particular, thin films, alternative methods must be developed. One such alternative is the use of nuclear resonance as an energy analysis technique. This approach was introduced in

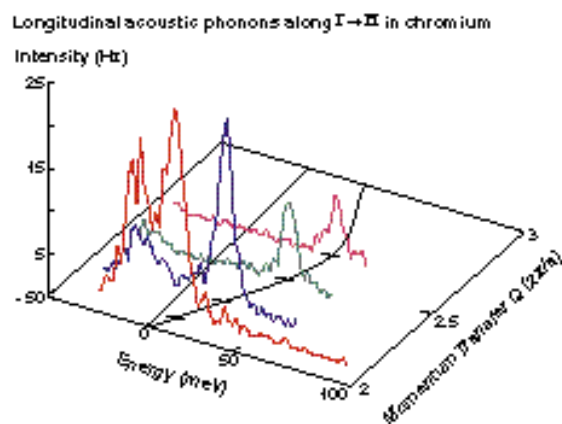


Fig. 5.56 Studies of phonons in chromium, demonstrating the performance of the instrument for high-resolution inelastic x-ray scattering.

1994 (Seto et al., 1995; Sturhahn et al., 1995; Chumakov et al., 1996b), and it relies on tunable high-energy-resolution monochromators and the presence of suitable isotopes in the sample under analysis. This technique provides unequalled capability in terms of measuring partial phonon density of states in any medium, solid or liquid, crystalline or amorphous, bulk or thin films—even monolayers at an interface. It also allows extraction of phonon density of states directly from the data without the knowledge of crystal structure. During the 1997-98 period, the inelastic nuclear resonant scattering studies continued using Fe and have been extended to Sn and Eu isotopes. There were many experiments in thin films, monolayers at interfaces, samples under high pressure, biological samples at low temperatures and amorphous materials. For example, we have demonstrated that this method can be utilized to study the effect of reduced dimensionality on vibrational modes. In this instance, we measured phonon density of states of nanocrystalline iron (Fultz et al., 1997).

A brief description is provided below of the vibrational behavior of Fe/Cr multilayered systems. For this purpose, it was envisaged to measure the vibrational density of states (VDOS) at different locations in a multilayer through the elemental selectivity inherent with this technique. In recent literature, the method of obtaining the phonon spectrum of a system involving nuclear resonance as an energy analyzer is referred to as PHOENIX (PHOnon Excitation by Nuclear Inelastic absorption of X-rays). In this study, monolayers of ^{57}Fe were placed either in the center of an iron layer or at a Cr-Fe interface. The iron layers themselves consist of ^{56}Fe to suppress any unwanted effects

due to the 2% abundance of ^{57}Fe in natural iron. In this experiment, a newly developed "nested monochromator" with an energy resolution of 2.1 meV was used. This device represents considerable improvement in energy resolution compared to the previous 5.5-meV monochromator while maintaining ample photon flux. In addition, incident and exit beams remain parallel, which is quite advantageous in thin-film experiments of this type. The samples were prepared in Duisburg by evaporation under UHV conditions. A properly cleaned MgO substrate was coated with a 50 Å Cr buffer layer. The deposition sequences are then $200\times[^{57}\text{Fe}(1\text{Å})/^{56}\text{Fe}(11.5\text{Å})/\text{Cr}(11.5\text{Å})]$ (probe layer at the interface, type I), $200\times[^{56}\text{Fe}(5.7\text{Å})/^{57}\text{Fe}(1\text{Å})/^{56}\text{Fe}(5.7\text{Å})/\text{Cr}(11.5\text{Å})]$ (probe layer at the center, type C). All of the six provided samples (2 of type C and 4 of type I) were investigated, and the VDOS were determined successfully. The VDOS of the type C samples and bulk-iron (alpha phase) are virtually identical. However, when the ^{57}Fe -probe layer is placed at the interface (type I samples), significant changes in the VDOS are observed. High-energy phonon modes (35 meV, supposedly near the Brillouin zone) are clearly suppressed. On the other hand, the density of medium-energy modes, particularly around 23 meV, is visibly enhanced. The experimental results clearly demonstrate the validity of the PHOENIX technique when applied to vibrational dynamics of thin films. The illuminated amount of probe material (^{57}Fe) was only about 5 micrograms. Similar measurements were taken in Fe/Au multilayer systems with varying thicknesses of Fe layers to investigate the effect of the presence of heavy atoms. Partial phonon density of states of Fe in this multilayer system is shown in Fig. 5.57.

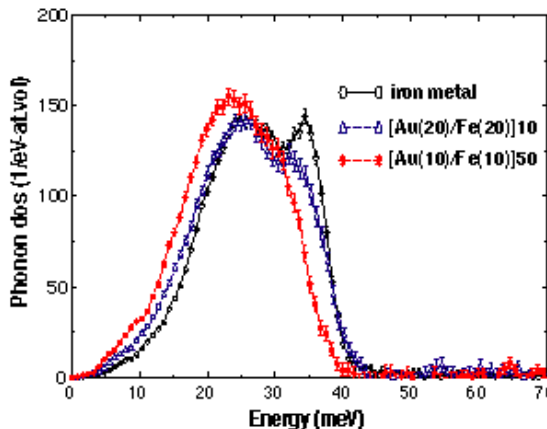


Fig. 5.57 Phonon density of states of Fe in an Fe/Au multilayer with varying thicknesses. As the layer thickness decreases, the softer modes below 25 meV appear to gain. Also note the disappearance of the longitudinal acoustic mode at 36 meV. Similar trends were observed with decreasing thickness in pure iron films. (Work in progress, in collaboration with S. Bader of Argonne National Laboratory.)

The phonon density of states of Sn metal under high pressure has been measured using inelastic nuclear resonant scattering. The pressure calibration of the diamond anvil was done using sector 13, GEO-CARS facilities. We used 23.87-keV x-rays both to excite the ^{119}Sn nuclear resonance and to observe the delayed signal. Two specially designed APD detectors enabled a count rate of a few Hz, which was sufficient to record three spectra in 3 days at 8, 15, 20 GPa pressures. The total volume of sample illuminated was 0.05 mm^3 . This was also the first time we have employed a third asymmetric crystal to reduce the vertical beam size, so the energy scans required coordinated motion of all three crystals. The energy resolution for this measurement was 3.7 meV. This was a first demonstration of the feasibility of phonon density of states measurements under high pressure using

PHOENIX. Phase transitions under high pressure will be the focus of future investigations.

Soon other users with systematic research programs can begin their work at beamline 3-ID. In preparation, we have completed a data acquisition system in the lab for users to try to learn our beamline system motion control and data acquisition system. Also, some critical data analysis software was developed to allow users to extract phonon density of states from experimental data.

5.4.5 Sector 4

Introduction

In 1997, it was decided to extend and enhance the capabilities of SRI-CAT by building a new sector whose primary purpose will be to exploit the polarization properties of radiation, an area that other CATs have limited plans to pursue.

The objective of this sector is to develop instrumentation and techniques that will utilize the high brilliance, variably polarized x-ray beams produced from two APS undulators and will also perform high-heat-load testing and diagnostics for Phase-2 FE and optical components. Two separate branch lines covering the “soft” (0.5 – 3 keV) and hard (>3 keV) x-ray regions are planned. One of the key components for the new sector will be a circularly polarized soft x-ray undulator. (The CPU is described in detail in section 5.1.3.) This is necessary because manipulation of beam polarization is not possible at energies between 1 and 2 keV using optical phase retarders. In the hard x-ray region, undulator A will be used

with crystal optics, such as transmission Bragg and Bragg-Laue phase retarders.

Transferring the hard x-ray polarization programs from sector 1 and the soft x-ray spectroscopy program from sector 2 will allow for improved sharing of beam time among all four SRI-CAT sectors. It will also give a clearer definition of the SRI-CAT sector structure. Sector 1 will specialize in high-energy x-ray optics development and time-resolved experiments, sector 2 will be the imaging and coherence techniques sector, sector 3 will remain as is: meV and nano-eV techniques, and sector 4 will become a polarization techniques sector with capabilities for testing components that have to withstand high heat loads. Another important aspect is that SRI-CAT will be able to make efficient use of the financial contributions from the X-ray Physics Group and the Australian Group, giving them and outside users improved accessibility to all of the SRI-CAT scientific resources.

The three major programs targeted for this new sector are:

1. Development of 0.4-3 keV instrumentation for high-spectral-resolution/ high-photon-flux polarization-dependent spectroscopy programs. This will be achieved with an elliptically polarized undulator and a polarization-preserving grazing-incidence monochromator. The scientific program will cover magnetic circular dichroism (MCD), resonant magnetic scattering, spin-resolved photoemission, and x-ray fluorescence. An important aspect of this program is that this energy range covers the transition metal and rare earth L and M edges, respectively, as well as numerous important elements, such as the O K, Cu L, and Si K edges.
2. Development of polarizing optics and techniques for the 3-100 keV x-ray energy range. This program will use a plane-polarized x-ray beam from undulator A together with polarization-manipulating crystal optics. The scientific program will cover resonant and non-resonant magnetic scattering, magnetic circular dichroism, magnetic reflectivity, and magnetic Compton scattering.
3. Development of high-heat-load FE and optical components for use with storage ring currents up to 300 mA. This program will use an experimental chamber as close to the shield wall as possible for thermal cycling of FE and beamline components.

In order to accomplish the objectives of the three programs outlined above, the spectral requirements outlined in Table 5.6 must be met.

In order to provide x-rays from 0.4-100 keV with high brilliance, two undulators will be installed in the sector 4 straight section. Both devices will be 2.4 m long. The hard x-ray range will be covered using undulator A. A custom 12.8-cm-period CPU will primarily be used for the soft x-ray range. Figure 5.6 shows the brilliance range of the soft x-ray device in the linear polarization mode, together with a 5.0-cm-period elliptical device planned for the Advanced Light Source. The 12.8-cm device has been described in section 5.1.3 of this report.

A key innovation of this beamline was the proposed operation of two undulators simultaneously, supplying radiation to two independent branch lines, one for hard x-ray experiments and the other for soft x-ray

Table 5.6 Spectral Requirements for the Scientific Programs in Stations 4-ID-A (FOE), 4-ID-B, and 4-ID-C

	4-ID-A (FOE)	4-ID-B	4-ID-C
Spectral Range (keV)	-	3-100	0.4-3.5
Resolving Power	-	10,000	2,000-12,000
Beam Size @ Station (mm)	3	0.2 - 3	1
Flux /0.1% BW	-	10^{14}	10^{13}
Source Polarization	-	H	H, V, LCP, RCP
Total Power (kW)	6		
Power Density (W/mm ²)	230		

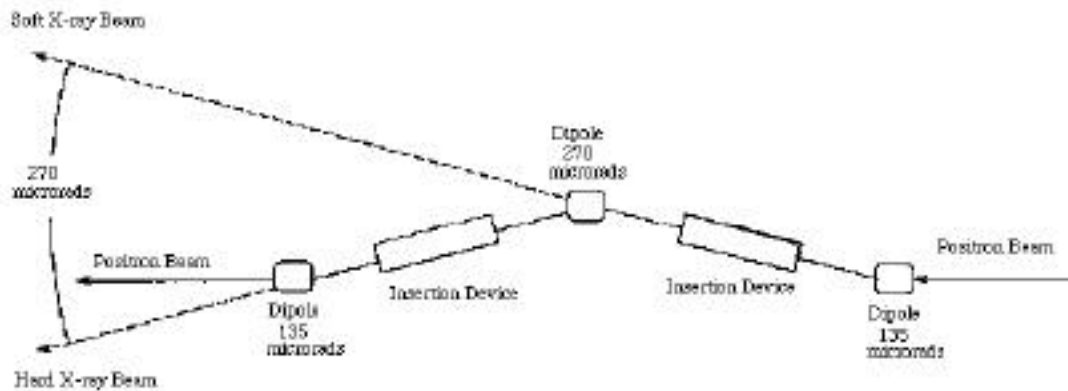


Fig. 5.58 Sector 4 insertion device plan.

studies. The beams from the two undulators will be spatially separated by introducing an angular deviation of the positron beam between the devices (Fig. 5.58). An initial estimate requires an 8-mm beam separation in the FOE at approximately 30 meters from the center of the straight section. This will require a dipole electromagnet sufficient to steer the beam through 267 microradians, which is technically achievable (Decker, 1998).

Layout of the Sector

The ID beamline consists of two branch lines that share the same first optical enclosure (FOE), 4-ID-A. The optical design of this sector is based on eight considerations:

1. Spatially separated undulator beams for simultaneous operation of both branch lines

2. Access to white beam (undulator A) directly adjacent to the shield wall for thermal loading tests
3. A windowless front end for access to soft x-ray energies
4. Access to white beam in a hutch beyond the FOE
5. A clear path beyond the white-beam hutch for possible extension of the hard x-ray branch line
6. Use of a grazing-incidence soft x-ray monochromator for presentation of the soft x-ray source polarization
7. Simple vacuum mechanical design for minimum downtime of both lines
8. Maximum utilization of available floor space

Layout of the ID Beamline

The ID beamline is split into two branch lines to optimize the utilization of the 0.5-30 keV undulator radiation (Fig. 5.58). The rationale for this branching is described in the first part of this section. The ID beamline is divided into three functional parts. The three parts are the first optics enclosure and the two branch lines, which are described separately below.

Beamline Branching

Our plan is to branch the two end stations, 4-ID-B and 4-ID-C, by spatially separating

the undulator beams. The outboard (hard x-ray) beam will pass through the FOE undeviated to the hard x-ray white-beam station (4-ID-B). The inboard (soft x-ray) beam will be deflected outward to branch line 4-ID-C using a pair of horizontally deflecting mirrors. (See Fig. 5.17 for a layout of the beamline.) The incidence angle onto each mirror is 1.25° giving a total deflection of 5° .

Major considerations for beam branching include:

- the compatibility of beamline optical components that are required for the different scientific programs in terms of polarization preservation, monochromator resolving power in the required energy range, mirror focusing requirements and monochromator dispersion plane requirements; and
- the engineering and construction of these optical components, thermal management of these optical devices, together with other aspects, such as beamline vacuum and radiation-shielding requirements, and overall operation of the two branches.

The hard x-ray branch line is designed for polarization manipulation in the 3-100 keV x-ray energy range. This will be achieved by using crystal optics following the DCM.

The soft x-ray branch line is designed to preserve the source polarization properties and to deliver an x-ray beam of high energy resolution in the 0.4-3.5 keV energy spectral region. This branch will be used for high-resolution polarization-dependent spectroscopy.

Beamline Component Test Facility with Movable Mask

The sector 4 FOE will also accommodate a 1.75-m-long vacuum chamber for a beamline component test facility (BCTF). The chamber will be equipped with large access flanges for insertion of a variety of test components, such as white-beam photon shutter blades, white-beam masks, or white-beam slits. Numerous smaller flanges will be used for thermocouple, electrical and water-cooling feedthroughs, infra-red camera and visible light viewports and actuator ports to vary the angle of incidence on the component under test.

In order to test high-heat-load components, the BCTF chamber will be vented and the component will be mounted on an actuation stage. At this time, a fixed mask and photon stop will be mounted and locked in position on the downstream wall of the BCTF chamber. The photon stop will be designed for a maximum 6-kW total beam power with 400 W/mm² heat flux.

Soft X-ray Horizontally Deflecting Mirrors

To deliver undulator radiation to the soft x-ray branch line (4-ID-C), two horizontal deflection mirrors located at approximately 29.9 meters will be inserted into the beam and will deflect the undulator radiation outboard 5° (1.25° incidence angle onto each mirror).

The incidence angle of 1.25° results from the compromise between reasonably high reflectivity for 0.4-3.5 keV x-rays for several mirror materials and sufficient separation between the two branch lines for

placement of optical elements upstream. The mirrors will be coated with Rh, which has a cut-off energy of 2.6 keV. Multilayers will be used to reach higher energies.

The maximum total power and power density on the first mirror surface are 28.6 W and 0.9 W/cm², respectively. The equivalent mirror designed for the 2-ID-C branch line has an absorbed power one decade higher and a power density two decades higher. Therefore we do not consider this to be a concern in the sector 4 design.

Hard X-ray Branch Line 4-ID-B

The hard x-ray branch line is designed for polarization manipulation in the 3-100 keV x-ray energy range. The primary goal of this beamline is to use the linearly polarized beam from undulator A and convert it to circularly polarized beam by using phase retarding crystal optics. Depending on the energy range, different schemes will be used (Lang et al., 1996). In the energy range up to 20 keV, a DCM will be used in conjunction with either perfect diamond or silicon phase retarders. In the energy range above 20 keV, a germanium phase retarder will be used. A mirror following the DCM will focus radiation in the vertical direction.

Double-Crystal Monochromator (DCM)

The DCM is the first optical component that is exposed to high-heat-load conditions. Liquid nitrogen cooling of crystals will be implemented, as in the 1-ID beamline.

Focusing Mirror

The function of this mirror is to vertically focus radiation into the end station. Since the mirror is placed after the monochromator, substrate cooling is not required. The shape of the mirror is cylindrical, with a radius that can be varied in order to achieve maximum flexibility in focusing.

0.4-3.5 keV Soft X-ray Spectroscopy Branch Line 4-ID-C

The 4-ID-C branch line will be dedicated to spectroscopy and instrument development in the intermediate energy range from 0.4 to 3.5 keV. The principal aim of this beamline is to preserve the undulator source polarization. It will also maximize flux throughput at relatively high resolving powers, of the order of several thousand. The source polarization will be preserved by using grazing angles of incidence. The entire branch line upstream and including the Y5 vertical focusing mirror assembly will be transposed directly, as is, from branch line 2-ID-C. The only re-engineering involved for this branch line will be the Y4 double mirror assembly. Also a new vertical mirror will be required because of the modified source-to-mirror distance, however the mechanical assembly from the existing sector 2 beamline will be used.

At the end station, a flexible UHV experimental chamber will be used. Currently a two-tier UHV experimental chamber is under testing. This will be used

for thin film and multilayer, as well as gas phase, studies. The monochromatic beam will enter the bottom analysis chamber, which is equipped with a Perkin Elmer hemispherical analyzer with a mean radius of 140 mm, an acceptance angle of $\pm 20^\circ$ and multichannel electron detector, and an electron gun with 1000-Å beam diameter. The top preparation chamber will be equipped with a reverse-view LEED, an electron gun and hemispherical analyzer for Auger analysis, two thin-film deposition sources, a quartz-crystal thin-film deposition monitor, and an ion sputter gun. Thin-film samples prepared in the upper chamber will be transported into the lower analysis chamber by a precision 600-mm-travel linear manipulator that also has liquid nitrogen and resistive heating capabilities. An electron spin detector will be added to one of the hemispherical analyzers in the near future. In collaboration with the adjacent imaging/coherence beamlines 2-ID-B and 2-ID-E, we also plan to implement a zone-plate-based photoelectron microscope with a spatial resolution of approximately 1 micron.

A photoelectron conversion microscope with a spatial resolution of less than 20 nm is also being considered. To achieve these levels of stability, an environmental enclosure to minimize acoustic vibrations will be required.

In May of 1998, the MOU for sector 4 was signed and shortly thereafter construction commenced. The first beam in the FOE is planned at the beginning of 1999. The sector 4 construction and commissioning schedule is presented in Table 5.7.

